

Asteroseismic ages for 17,000 stars in *Kepler*, K2 and TESS

Emma Willett,^{1*} Andrea Miglio,^{2,3,1} Saniya Khan,⁴ Yvonne Elsworth,¹ Benoît Mosser,⁵ Karsten Brogaard,^{2,6} Giada Casali,^{7,8,2,3} Cristina Chiappini,⁹ Valeria Grisoni,^{10,2} Amalie Stokholm,^{1,2,3,6} Diego Bossini¹¹ and William J. Chaplin¹

¹ School of Physics and Astronomy, University of Birmingham, Edgbaston, Birmingham, B15 2TT, UK

² Dipartimento di Fisica e Astronomia, Università degli Studi di Bologna, Via Gobetti 93/2, I-40129 Bologna, Italy

³ INAF - Osservatorio di Astrofisica e Scienza dello Spazio di Bologna, Via Gobetti 93/3, I-40129 Bologna, Italy

⁴ Institute of Physics, École Polytechnique Fédérale de Lausanne (EPFL), Observatoire de Sauverny, 1290 Versoix, Switzerland

⁵ LIRa, Observatoire de Paris, Université PSL, CNRS, Sorbonne Université, Université Paris Cité, CY Cergy Paris Université, 92190 Meudon, France

⁶ Stellar Astrophysics Centre, Department of Physics & Astronomy, Aarhus University, Ny Munkegade 120, 8000 Aarhus C, Denmark

⁷ Research School of Astronomy & Astrophysics, Australian National University, Cotter Rd., Weston, ACT 2611, Australia

⁸ ARC Centre of Excellence for All Sky Astrophysics in 3 Dimensions (ASTRO 3D), Stromlo, Australia

⁹ Leibniz-Institut für Astrophysik Potsdam (AIP), An der Sternwarte 16, D-14482 Potsdam, Germany

¹⁰ INAF, Osservatorio Astronomico di Trieste, via G.B. Tiepolo 11, I-34131, Trieste, Italy

¹¹ Department of Physics and Astronomy G. Galilei, University of Padova, Vicolo dell’Osservatorio 3, I-35122, Padova, Italy

Accepted XXX. Received YYY; in original form ZZZ

ABSTRACT

The availability of asteroseismic constraints for tens of thousands of red giant (RG) stars has opened the door to robust age estimates, enabling time-resolved studies of different populations of stars in the Milky Way. This study leverages data from *Kepler*, K2, and TESS, in conjunction with astrometric data from *Gaia* DR3 and spectroscopic constraints from APOGEE DR17 and GALAH DR3, to infer parameters for over 17,000 RGs. We use the code PARAM to homogeneously infer stellar properties considering in detail the sensitivity of our results to different choices of observational constraints. We focus on age estimation, identifying potentially unreliable age determinations, and highlight stars with unreliable $\Delta\nu$ measurements based on comparisons using *Gaia* luminosities. These are particularly relevant in K2 data due to the short duration of the observations of each campaign, and therefore important to characterise for Galactic archaeology studies where the spatial range of K2 is a benefit. Thanks to the combination of data from different missions we explore trends in age, mass, and orbital parameters such as R_g and Z_{\max} , and examine time-resolved $[\alpha/M]$ - $[\text{Fe}/\text{H}]$ planes across different Galactic regions. Additionally, we compare age distributions in low- and high- α populations and chemically selected *ex situ* stars. The study also extends known mass- $[\text{C}/\text{N}]$ ratio relationships to lower masses. The catalogues resulting from this work will be instrumental in addressing key questions in Galactic archaeology and stellar evolution, and to improve training sets for machine-learning-based age estimations.

Key words: asteroseismology – Galaxy: abundances – Galaxy: evolution – Galaxy: stellar content – stars: abundances – stars: kinematics and dynamics

1 INTRODUCTION AND MOTIVATION

Long-duration, space-based photometry has provided precise asteroseismic constraints for tens of thousands of red giant (RG) stars. These constraints, when combined with measurements of effective temperature and metallicity, have paved the way for robust estimates of stellar properties - including the mass, which is key for understanding stellar evolution, Galactic stellar structures and exoplanet systems. As a result of the tight correlation between initial stellar mass and main sequence (MS) lifetime, we can now obtain age estimates for large samples of RG field stars. These reliable stellar masses and ages throw light on open questions of stellar structure and evolution as well as providing strong tests of stellar models (see e.g. Chaplin & Miglio 2013; Aerts 2021, for reviews). In addition,

robust age estimates combined with spectroscopic and astrometric information are opening the door to understanding the formation and evolution of the Milky Way (MW) through Galactic archaeology (e.g., see Freeman & Bland-Hawthorn 2002; Matteucci 2021).

For meaningful studies of our Galaxy, we require samples which reach different Galactic domains, extending as far as possible both spatially and temporally. Low-mass RGs are excellent candidates for this work, being intrinsically luminous and long-lived, they can be seen over several kpc and probe more than 10 Gyr of MW history. Asteroseismic constraints have been used in this context in the Galactic disc (e.g. Miglio et al. 2013; Casagrande et al. 2016; Anders et al. 2017; Silva Aguirre et al. 2018; Rendle et al. 2019; Sharma et al. 2019; Miglio et al. 2021; Stokholm et al. 2023; Willett et al. 2023; Schonhut-Stasik et al. 2024; Valle et al. 2024; Warfield et al. 2024) and the halo (e.g. Valentini et al. 2019; Chaplin et al. 2020; Grunblatt et al. 2021; Matsuno et al. 2021; Montalbán et al. 2021; Borre

* E-mail: e.m.willett.bham.ac.uk

et al. 2022). Ages from asteroseismology have also been used to verify other age-estimation techniques, such as chemical clocks and gyrochronology of main sequence stars (e.g. Hall et al. 2021; Morel et al. 2021; Moya et al. 2022), and as training data for machine learning techniques (Mackereth et al. 2019b; Ciucă et al. 2021; Anders et al. 2023; Leung et al. 2023). The latter, in particular, represents a powerful way to vastly increase the sample of stars with age information available but relies on high-quality training data, and inferences made by extrapolating beyond the parameter space covered by the training set are unlikely to be reliable. For this reason, increasing the number and variety of stars with robust, homogeneously determined ages from more ‘direct’ methods, like asteroseismology, will support efforts to answer open questions about the MW and the stars in it on a large scale.

In this work, we present reliable ages for over 17,000 stars, based on *Kepler*, K2 and TESS photometry, APOGEE and GALAH spectroscopy and *Gaia* astrometry. We show that asteroseismic results from the three photometry missions are complementary, with each representing a different compromise between the precision of the observations and scale of the coverage. We provide stellar and orbital parameters which are homogeneously determined across the samples, and consider in detail the sensitivity of our results to different choices of observational constraints. We also explore the applicability of each set of parameters to different problems, showing that the evolutionary phase of the star can affect the reliability of its age estimate, and provide quality flags to combat this effect. We use our samples to explore several well-known chrono-chemo-kinematic relations in Galactic archaeology studies, showing trends with age in kinematic and chemical properties which we find to be robust against the uncertainties in the stellar parameters. Such trends may be used to constrain the dynamical and chemical evolution of the MW, and the K2 dataset, including stellar and orbital parameters, presented in this work has already been utilised in this context to study the radial metallicity gradient of the thin disc (Willett et al. 2023), cerium enrichment (Casali et al. 2023), and young α -rich stars (Grisoni et al. 2024), while the *Kepler* and K2 samples have been used to investigate mass loss during the red-giant-branch phase (Broggaard et al. 2024). We also identify the stars in our sample which were likely born outside the MW and present some results on stellar evolution during the RG phase, thus addressing open topics in both Galactic archaeology and stellar physics.

This paper is organised as follows: in Section 2 we present the observational data and describe the cross-matched samples, and we describe the inference of stellar and orbital parameters in Section 3. Section 4 presents some applications of our results, in both Galactic archaeology and stellar evolution. A brief summary is provided in Section 5.

2 OBSERVATIONAL CONSTRAINTS

The catalogues compiled in this work are based upon asteroseismic observations from the *Kepler* (Borucki et al. 2010; Gilliland et al. 2010), K2 (Howell et al. 2014) and TESS (Ricker et al. 2015) missions. These are combined with astrometric parameters from *Gaia* DR3 (Gaia Collaboration et al. 2016, 2023) and spectroscopically derived quantities from APOGEE DR17 (Majewski et al. 2017; Abdurro'uf et al. 2022) and GALAH DR3 (De Silva et al. 2015; Sharma et al. 2019; Buder et al. 2021). In Sections 2.1 - 2.3 we introduce the observations, required parameters and quality flags and cross-match procedure, and describe the final samples in Section 2.4.

2.1 Asteroseismic constraints

In this work, we make use of the global asteroseismic parameters ν_{\max} , the frequency of maximum oscillation power, and $\Delta\nu$, the average large frequency separation. These parameters are related to the surface gravity and mean stellar density, respectively, so can be used to infer the stellar mass and radius (see Chaplin & Miglio 2013). In the following sections, we outline some relevant details of each asteroseismic mission and how ν_{\max} and $\Delta\nu$ are obtained.

2.1.1 Kepler

The NASA *Kepler* mission provided 4 years of observations from 2009 for a single 105 deg² field of view. Our sample is based on the catalogue of Yu et al. (2018), which contains more than 16,000 RGs. These stars were selected from six previously published catalogues, but the lightcurves were reanalysed to produce a set of homogeneously determined ν_{\max} and $\Delta\nu$ values which we adopt in this work. Evolutionary states are also provided for some stars and, where available, determine which models are used in PARAM (Section 3.1). To this catalogue, we add the 2MASS ID and magnitudes available in the *Kepler* Input Catalogue (KIC, Brown et al. 2011).

2.1.2 K2

Following the failure of *Kepler*’s second reaction wheel in 2013, the mission was repurposed as K2, which went on to observe 20 campaigns around the ecliptic plane, each of 80 days duration (see Sharma et al. 2022, for a description of the selection function). Here we use lightcurves produced by the EVEREST pipeline (Luger et al. 2018), analysed with two independent methods. The pipeline of Elsworth et al. (2020, hereafter BHM), uses ν_{\max} determined by the deep learning method of Hon et al. (2018a,b) as a soft prior, and then applies several layers of weak tests to exclude false results without removing real, but unusual, stars. Mosser & Appourchaux (2009) and Mosser et al. (2010) provide an alternative pipeline (hereafter COR) and, in general, the results of these two approaches agree well (see Appendix A). In the interest of clarity, the results presented here focus on the BHM pipeline, as Mackereth et al. (2021) found that it produces fewer false positive detections and the definition of $\Delta\nu$ is more similar to that used in our models. We add the 2MASS ID and magnitudes from the Ecliptic Plane Input Catalogue (EPIC, Huber et al. 2016), removing cases where a single 2MASS ID is mapped to multiple K2 IDs. Because some targets were observed in multiple K2 campaigns, we also add a flag to identify the observation to be retained in our analysis, to prevent double counting when utilising our samples. We retain targets with a higher SNR on ν_{\max} , meaning that the flag may be different for the BHM and COR pipelines.

2.1.3 TESS

TESS was launched in 2018 and will survey the whole sky with repeated 27 day observations of 96 \times 24 deg sectors. In this work, we use on the results from the southern continuous viewing zone (SCVZ), where these sectors overlap, from the first year of observations. Mackereth et al. (2021) extracted lightcurves from the full frame images, which were analysed by three asteroseismic pipelines. Here, we focus on the results from the BHM pipeline.

2.1.4 Cuts in asteroseismic parameters

We apply two cuts in the asteroseismic observables. First, we remove targets with ν_{\max} more than three standard deviations below 20 μHz , to mitigate contamination by early-AGB stars where we cannot robustly determine the age, and as asteroseismic inference based on global asteroseismic parameters has not undergone the same robust testing as for less evolved targets. It should be noted that this cut also removes some evolved Red Giant Branch (RGB) targets, which would be an important consideration in the comparison of age distributions drawn from these observations and models of the chemo-dynamical evolution of the Milky Way. Since that is not the focus of this work, we do not address it further here. Second, we remove targets where ν_{\max} may be affected by the Nyquist frequency of the observations. Such cases are identified by comparing ν_{\max} and $\Delta\nu$ and removing targets where the tight correlation between these quantities is broken – i.e. where $\Delta\nu$ is too large for the measured ν_{\max} . In practice, this means removing targets with $\Delta\nu \geq 21 \mu\text{Hz}$ (see Appendix B).

2.2 Astrometric constraints

We obtain the required astrometric constraints from *Gaia* DR3, which is based on 34 months of observations. We use five-parameter solutions $[\alpha, \delta, \varpi, \mu_\alpha, \mu_\delta]$ and, following Lindegren (2018), remove targets with $\text{ruwe} > 1.4$ or which are marked as binaries by the `non_single_star` flag. We also consider different corrections to the known zero-point offset in *Gaia* parallaxes (Lindegren et al. 2021). Khan et al. (2023) compared the *Gaia* parallaxes with an independent estimate based on asteroseismology and found that the correction of Lindegren et al. (2021) works well for the *Kepler* field but significantly overestimates the zero-point offset in K2 (averaged over multiple campaigns) and underestimates it in the TESS SCVZ. In addition, they also found a significant trend in parallax difference with stellar mass in some K2 campaigns. Though the underlying cause is not clear, it may be related to the different noise levels of the K2 campaigns, the variation in the quality of the *Gaia* data as a result of the scanning law, and the accuracy of the seismic parameters. For this reason, in this work, we apply the Lindegren et al. (2021) correction to the *Kepler* and TESS sample, but use a simpler constant correction of 17 μas for K2 (guided by the average offset found in quasars in DR3 by Lindegren et al. 2021, and the results of Khan et al. 2023). We test the sensitivity of our results to the zero-point correction in Section 3.1.

For the *Kepler* and K2 samples, we obtain the *Gaia* DR3 `source_id` via crossmatch to the `TMASS_PSC_XSC_BEST_NEIGHBOUR` table (Marrese et al. 2022), removing targets with multiple matches. The TESS SCVZ catalogue of Mackereth et al. (2021) already contains the DR2 `source_id` so we use the `DR2_NEIGHBOURHOOD` table instead (Mora et al. 2022). We retained sources with smaller angular separation in cases where a single DR2 `source_id` matches multiple DR3 results. Finally, for all samples, we obtain data from the DR3 `gaia_source` table, by matching on the `source_id`.

2.3 Spectroscopic constraints

The main spectroscopically derived parameters required in this work are the radial velocity (RV), effective temperature and chemical abun-

dances – specifically the iron abundance¹ and average α -element abundance.

2.3.1 APOGEE

We cross-match each asteroseismic sample with APOGEE DR17, which uses high-resolution ($R \sim 22,500$) infra-red (IR) spectroscopy to obtain stellar parameters and abundances from 20 elements, covering a range of nucleosynthesis channels. Chemical abundances and stellar parameters are obtained from the APOGEE Stellar Parameters and Chemical Abundances Pipeline (ASPCAP, García Pérez et al. 2016, and see Holtzman et al. in preparation for a full description of this pipeline as applied to APOGEE DR17). We remove targets with `STAR_BAD` or `STAR_WARN` set in `ASPCAPFLAG`, and those with any `RV_FLAG` set. In addition, when using any of the individual abundances we remove targets with the relevant `ELEM_FLAG` set. The uncertainties reported by ASPCAP reflect only the internal errors, so we enforce minimum values of $\sigma_{[\text{Fe}/\text{H}]} = 0.05 \text{ dex}$ and $\sigma_{T_{\text{eff}}} = 50 \text{ K}$ during the inference of stellar parameters (see Section 3.1).

Before crossmatching to APOGEE DR17, we remove duplicated observations of targets observed in multiple fields, retaining those with higher $[\text{Fe}/\text{H}]$ SNR. We then crossmatched based on the 2MASS ID (for TESS this was first obtained from `TMASS_PSC_XSC_BEST_NEIGHBOUR` table).

2.3.2 GALAH

We also cross-match the K2 samples to GALAH DR3 on the 2MASS ID, another high-resolution ($R \sim 28,000$) spectroscopic survey across the visible and IR. GALAH provides abundances for up to 30 elements per star (Kos et al. 2017), and we use the recommended quality flags, requiring that `snr_c3_iraf == 0`, `flap_sp == 0` and `flag_fe_h == 0` for all targets, and `flag_X_fe == 0` for other abundances X. While GALAH DR4 is now available (Buder et al. 2025), we report here the results for DR3 as they are investigated in other works where our APOGEE DR17 dataset is used (e.g. Khan et al. 2023; Grisoni et al. 2024) and the aim of this paper is to provide the full catalogues on which these other works are based.

2.4 Samples

In total, our samples contain observations of over 17,000 stars. Figure 1 shows their positions in Galactic spherical coordinates, with the full sample shown in black and the stars with reliable ages (see Section 3.1) overlaid in colours corresponding to the survey. In Figure 2 we show positions in Galactocentric Cartesian (top panel) and cylindrical coordinates (bottom panel). Finally, the samples are shown in APOGEE chemical abundance space using the well-studied $[\alpha/\text{M}]$ vs. $[\text{Fe}/\text{H}]$ plane² in Figure 3. For K2, we also show the GALAH $[\alpha/\text{Fe}]$ vs. $[\text{Fe}/\text{H}]$ plane, where the much greater scatter (expected due to the larger observational uncertainties) almost obscures the separation of the high- and low- α sequences.

¹ Throughout this work we use iron abundance as a tracer for metallicity: $[\text{Fe}/\text{H}] = \log_{10} (N_{\text{Fe}}/N_{\text{H}})_* - \log_{10} (N_{\text{Fe}}/N_{\text{H}})_{\odot}$, where N_{Fe} and N_{H} are the numbers of iron and hydrogen nuclei per unit volume of the stellar photosphere, respectively.

² We use $[\alpha/\text{M}]$ as a proxy for $[\alpha/\text{Fe}]$ as the differences between them (defining $[\alpha/\text{Fe}]$ as an average of $[\text{X}/\text{Fe}]$ for O, Mg, Si, S, and Ca) are negligible.

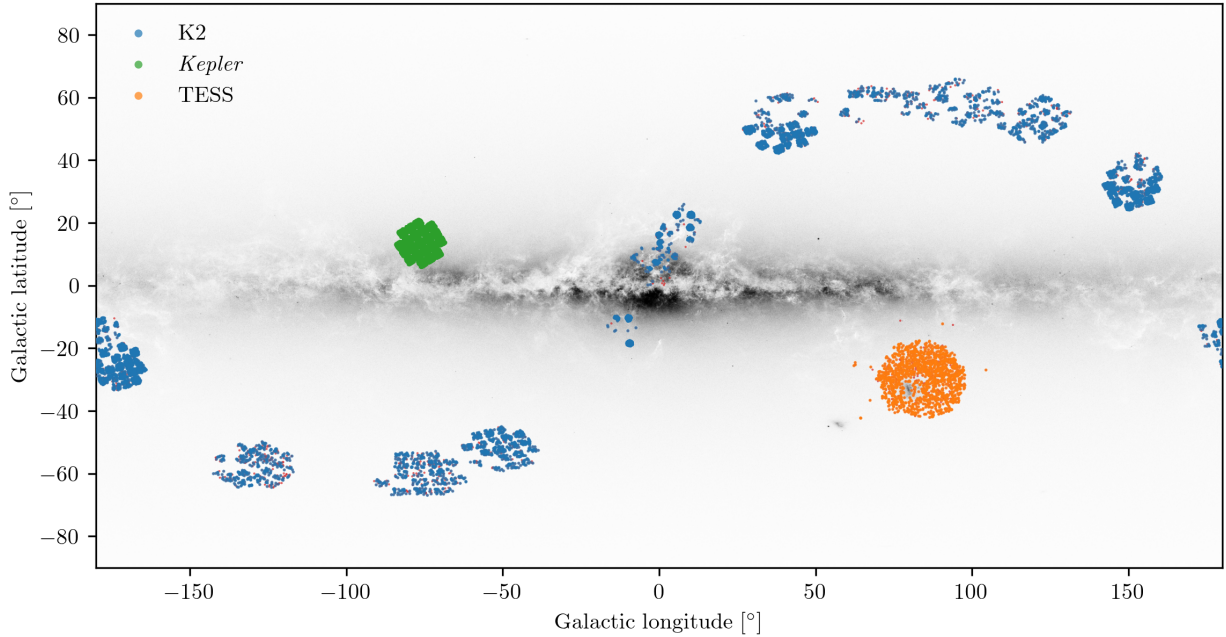


Figure 1. Location of stars in our samples in Galactic coordinates. Green, blue and orange points show stars with reliable ages from *Kepler*, K2 and TESS, respectively. Stars with reliable data but ages which do not pass our tests are shown with red points. In this figure we use distances from PARAM and reliability tests based on $\Delta\nu$. This figure was generated using `mwplot`^a, and the image in the background is modified from an image by ESA/Gaia/DPAC.

^a <https://milkyway-plot.readthedocs.io/en/latest/index.html>

3 INFERRING STELLAR AND ORBITAL PARAMETERS

From the observations described above, we infer stellar (Section 3.1) and orbital (Section 3.2) parameters for the stars in each sample. This section describes the assumptions made and, specifically in the case of the stellar masses and ages, the tests performed to ensure the most robust results are presented. In most cases, the figures shown in this section focus on the K2-APOGEE sample and additional figures corresponding to the *Kepler* and TESS samples can be found in the Appendix, where relevant. The catalogues are available online, and described in Appendix C.

3.1 Stellar parameters

Stellar masses (M_*), radii (R_*), ages (τ), and distances (D) are inferred using the PARAM code (da Silva et al. 2006; Rodrigues et al. 2014, 2017), which performs a Bayesian comparison between observations and a model grid. We follow the method presented in Miglio et al. (2021) using the law of Reimers (1975), with efficiency parameter $\eta = 0.2$ to estimate the mass loss during the ascent of the RGB (Miglio et al. 2012). We use the reference grid (G2) from Miglio et al. (2021), which was computed in MESA (Paxton et al. 2011, 2013, 2015, 2018, 2019) including microscopic diffusion and assuming a linear relation between the stellar helium and metal mass fraction ($\Delta Y / \Delta Z = 1.3$) and the same relative surface effects as in the Solar model (an alternative approach may be found in Li et al. 2023). Additional information about the model grid may be found in Rodrigues et al. (2017). For *Kepler* stars with evolutionary state determinations available, either RGB or core-He burning models are considered by PARAM as appropriate. For *Kepler* stars with unclassified evolutionary states, as well as stars from K2 and TESS, both sets of models are used. PARAM returns full posterior information, and we report the median and 16th and 84th percentiles here. We choose not to use evolutionary state information for the K2 and

TESS samples because we consider this to be the more conservative approach. To require an evolutionary state would significantly reduce the number of stars in our samples, and the subset remaining may be subject to additional biases. Moreover, by keeping the evolutionary state as unknown, we account for the associated uncertainty in a statistically consistent way rather than potentially biasing the sample toward stars with confidently determined states.

Observational constraints are provided by v_{\max} , T_{eff} , $[\text{Fe}/\text{H}]$ ³ and we test using either $\Delta\nu$ or the luminosity, L , based on the (zero-point corrected) *Gaia* parallax and 2MASS K_s photometry (Skrutskie et al. 2006, see Section 3.1.1). An uncertainty floor of $\sigma_{[\text{Fe}/\text{H}]} = 0.05$ dex and $\sigma_{T_{\text{eff}}} = 50$ K is imposed in the APOGEE observations, as the reported uncertainties reflect only the pipeline’s internal errors. In the case of T_{eff} , this has the additional benefit of reducing the impact of model uncertainties concerning the outer boundary conditions and near-surface convection. When using L as a constraint, to further mitigate the impact of the uncertain models’ T_{eff} scale on the inferred stellar parameters, we add the stellar mass estimated from the combination of the observed v_{\max} , L , and T_{eff} as an additional constraint (Section 3.1.1). This approach has been tested using stellar models computed with different surface boundary conditions and ensures that the inferred M_* is not significantly dependent on the models’ T_{eff} . The dependence of M_* on T_{eff} is explored further in Section 3.1.2.

For *Kepler* and K2 the luminosities were computed using extinctions from the Bayestar19 dustmap (Green et al. 2014, 2019) implemented in the `dustmaps` python package (Green 2018), from which we obtain quality flags for the convergence of the fit in each pixel and the reliability of the map at the queried distance. The TESS-SCVZ lies outside the range of Bayestar19, so we use the

³ $[\text{Fe}/\text{H}]$ is rescaled following the method of Salaris et al. (1993) for α -enhanced stars. See also the discussion in Miglio et al. (2021).

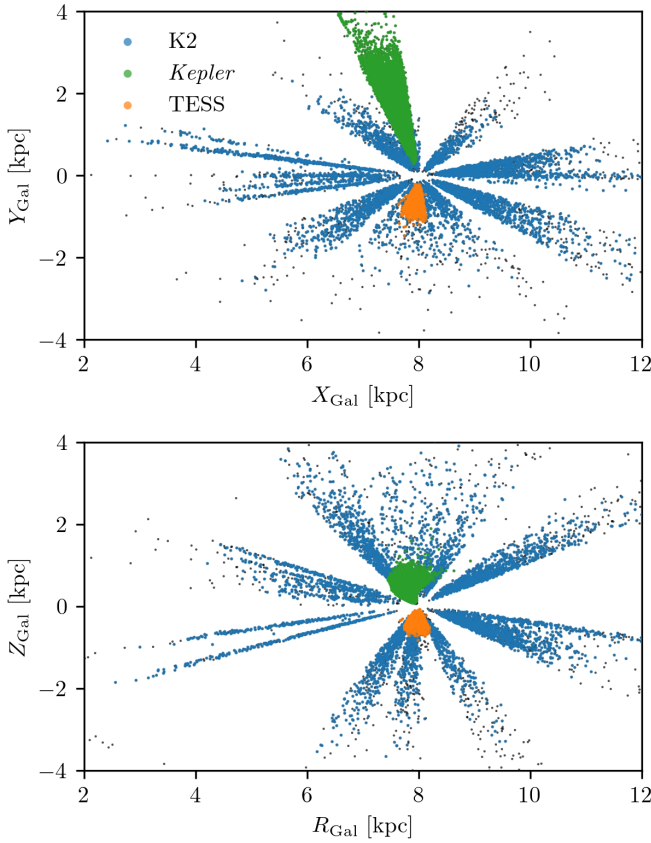


Figure 2. Location of stars in our sample in left-handed Galactocentric coordinates (top) and Galactocentric cylindrical coordinates (bottom). The colours are the same as Figure 1. In this figure we use distances from PARAM and reliability tests based on Δv .

combined19 dustmap (Drimmel et al. 2003; Marshall et al. 2006; Green et al. 2019) implemented in `mwdust` (Bovy et al. 2016) instead. In both cases, we require that $\varpi/\sigma_\varpi \geq 5$ when using the luminosities or quantities derived from the luminosity, and few stars are also removed by the range of validity of the bolometric correction computation, performed using the code of Casagrande & Vandenberg (2014, 2018).

As discussed in Section 1, several previous works have established ages for stars which overlap with those presented here. Of particular note, given the similar focus on applications to Galactic Archaeology, is the APO-K2 Catalogue of Warfield et al. (2024). We present a brief comparison between the APO-K2 ages and those determined in this work in Appendix E.

3.1.1 Using Δv or L as an observational constraint

In Figure 4 we show the stellar mass, M_* , and radius, R_* , obtained from scaling relations based on T_{eff} , ν_{max} and either Δv :

$$\frac{M_*}{M_\odot} = \left(\frac{\nu_{\text{max}}}{\nu_{\text{max}, \odot}} \right)^3 \left(\frac{\Delta v}{\Delta v_\odot} \right)^{-4} \left(\frac{T_{\text{eff}}}{T_{\text{eff}, \odot}} \right)^{\frac{3}{2}} \quad (1)$$

$$\frac{R_*}{R_\odot} = \frac{\nu_{\text{max}}}{\nu_{\text{max}, \odot}} \left(\frac{\Delta v}{\Delta v_\odot} \right)^{-2} \left(\frac{T_{\text{eff}}}{T_{\text{eff}, \odot}} \right)^{\frac{1}{2}}, \quad (2)$$

or L :

$$\frac{M_*}{M_\odot} = \frac{\nu_{\text{max}}}{\nu_{\text{max}, \odot}} \frac{L}{L_\odot} \left(\frac{T_{\text{eff}}}{T_{\text{eff}, \odot}} \right)^{\frac{-7}{2}} \quad (3)$$

$$\frac{R_*}{R_\odot} = \sqrt{\frac{L}{L_\odot} \left(\frac{T_{\text{eff}}}{T_{\text{eff}, \odot}} \right)^{-4}}. \quad (4)$$

In the Δv case (top panel) we see a strong feature with $M_* > 1.5 M_\odot$ and $R_* > 15 R_\odot$, which is not expected in descriptions of stellar evolution and is not present in the case where Δv is replaced by L (bottom panel). This is a consequence of the biases in ν_{max} and Δv which have previously been demonstrated in short-duration observations, such as K2 (c.f. Equations 1 and 2 and see also Tailo et al. 2022). We highlight stars which are common between the samples⁴ where $|M_{*, \Delta v} - M_{*, L}| > 0.5 M_{*, L}$ (red points, masses computed from Equations 1 and 3). In the Δv results, this highlights the high- M_* - high- R_* feature well, and from the L results we see from the clustering around $10 R_\odot$, $1 M_\odot$ that these stars are mostly members of the red clump (RC, and see also their position in the lower panel of Figure 9). This is an expected consequence of unreliable Δv determinations for core helium burning (CHeB) stars with short-duration asteroseismic observations (Tailo et al. 2022). Overlaid on the observations in large, black points is a simple demonstration of the effect of a bias in Δv . Starting from a star of $M_* = 1 M_\odot$ and $R_* = 11 R_\odot$, we decrease Δv in steps of 5% and recalculate the mass and radius from Equations 1 and 2. The mass and radius increase as the bias on Δv increases, following the high- M_* - high- R_* feature in the observations. In Appendix D we show that the situation is less significant when using the *Kepler* and TESS SCVZ samples, where the observation durations are much longer than the K2 campaigns. We flag and remove stars with a high mass difference in samples where Δv is an observational constraint, as their unreliable high masses will lead to erroneous, young ages.

In the remaining sample, we find that ages obtained from PARAM and Δv are less precise than those from L , thanks to the exquisite precision of the *Gaia* DR3 data (Figure 5). However, using L as a constraint introduces other sensitivities in the results which are discussed further, below.

Table 1 shows a summary of the samples from different sets of observational constraints. The number of stars with reliable data is higher in the Δv case because we do not require the additional checks on parallax uncertainty or dustmap flags. However, the number of stars with reliable ages in this case is smaller due to the removal of those with unreliable Δv values.

3.1.2 Ages from L : sensitivity to T_{eff} and ϖ -zeropoint

The mass, and therefore the age, from L is much more sensitive to T_{eff} , than when derived from Δv (compare Equations 1 and 3). Given the known offsets in the temperature scales between spectroscopic surveys (e.g. Hegedűs et al. 2023), this sensitivity is a limitation of the ages constrained by L . The scale of this effect is shown in Figure 6, where we plot the mass difference from the scaling relations using Δv (dark blue) or L (light blue) caused by decreasing T_{eff} by 50 K. For a $1 M_\odot$ star, the mass difference when using L is $\approx 5\%$, corresponding to an age difference of more than 1 Gyr.

⁴ There are some stars present in the Δv sample which are removed when using L as the observational constraint due to the quality flags on the extinction and parallax, described in Section 3.1.

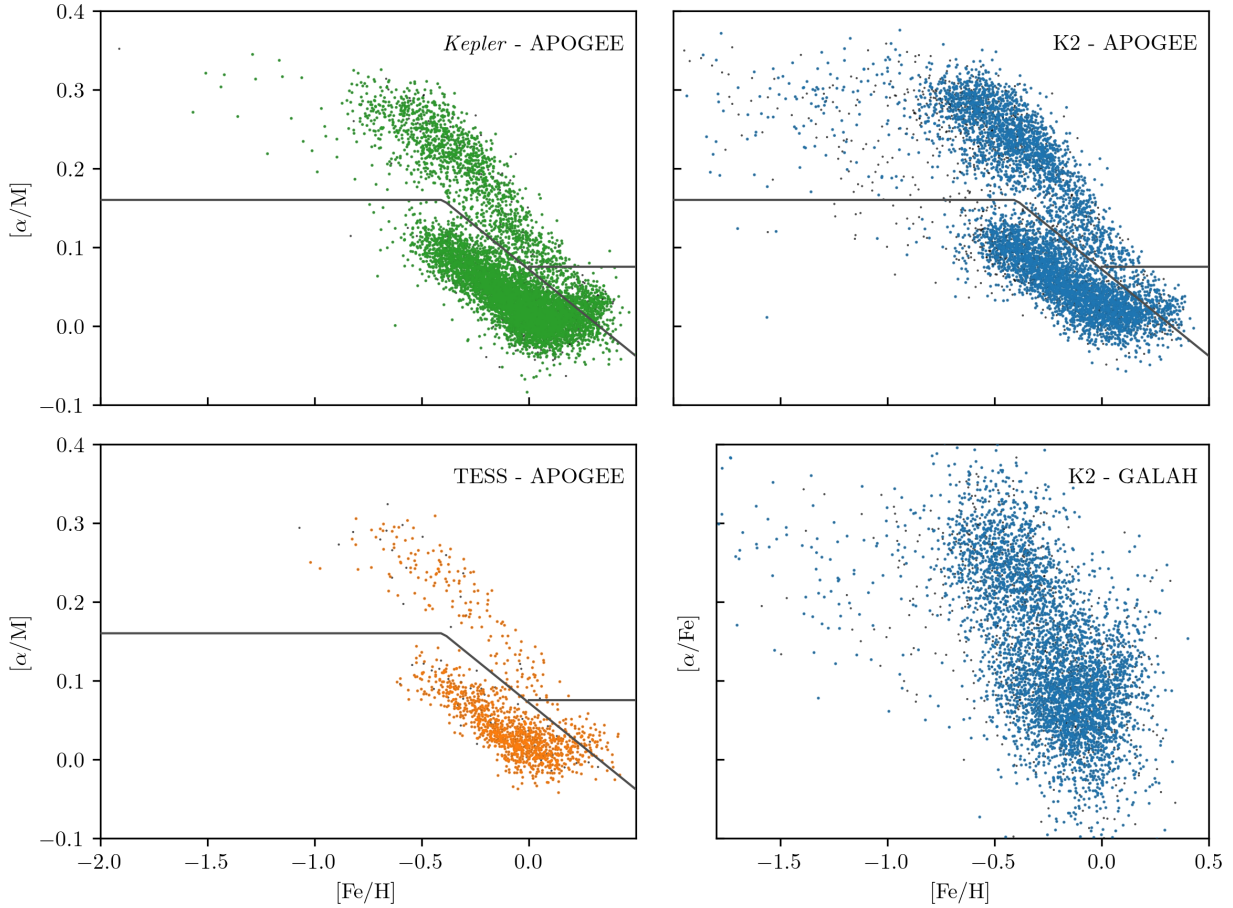


Figure 3. Average α element abundance $[\alpha/M]$ for APOGEE samples or $[\alpha/\text{Fe}]$ for the GALAH sample vs. $[\text{Fe}/\text{H}]$. The grey lines show the division between high-, low- and intermediate α populations used in Section 4.2. We have used reliability tests based on $\Delta\nu$ and the colours are the same as Figure 1.

Table 1. Summary of reliable targets in datasets with different observational constraints. See text for descriptions of the criteria for reliable data and age, τ . L_{17} and L_{Ldg} indicate the luminosity derived from $\varpi + 17$ μas or from ϖ corrected according to the scheme of Lindegren et al. (2021), respectively.

Photometry source	Asteroseismology pipeline	Spectroscopy source	Observational constraint	N_* with reliable data	N_* with reliable τ
<i>Kepler</i>	Yu 2018	APOGEE DR17	$\Delta\nu$	8199	7874
			L_{Ldg}	8105	7953
K2	BHM	APOGEE DR17	$\Delta\nu$	7390	6095
			L_{17}	6929	6896
			L_{Ldg}	7004	6968
	COR	GALAH DR3	$\Delta\nu$	5266	4486
			L_{17}	5056	5038
TESS	BHM	APOGEE DR17	$\Delta\nu$	7601	5751
			L_{17}	6883	6492
			$\Delta\nu$	1398	1313
			L_{Ldg}	1398	1379

Using the luminosity also introduces a sensitivity to the zero-point correction to the *Gaia* parallax. This is a further limitation and results in, effectively, data release-dependent ages. The situation is more complicated for K2, as Khan et al. (2023) found that the correction differs between K2 campaigns. In Figure 7 we show the difference in mass, again from the scaling relation (Equation 3) using the luminosity derived from $\varpi + 17$ μas , L_{17} , or with ϖ corrected according to the scheme of Lindegren et al. (2021), L_{Ldg} . Stars are coloured according to the logarithmic distance and sorted with the closest stars on top. As expected, more distant stars are more sensitive

to the zero-point correction, with a mass difference of more than 20% in some cases.

3.1.3 PARAM output: sensitivity to priors

Regardless of the choice of observational constraint, when using the stellar parameters output by PARAM, it is important to understand any effects which may be introduced by the model grid or choice of priors. When using $[T_{\text{eff}}, [\text{Fe}/\text{H}], \nu_{\text{max}}, L]$ as observational constraints, the stellar mass from PARAM is inferred based on the scaling relation of the same quantities (Equation 3), and any differences are

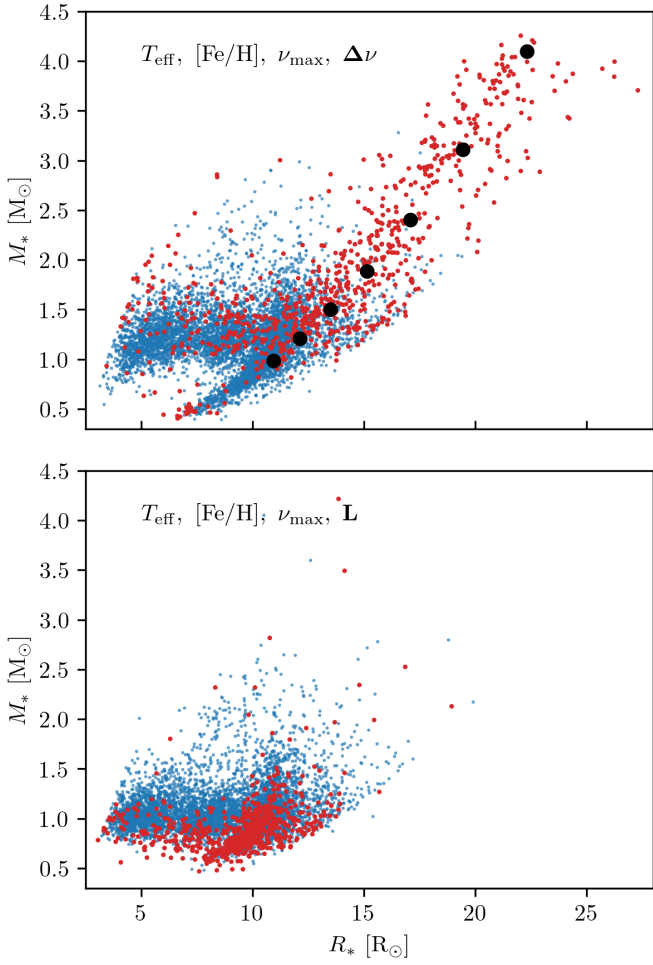


Figure 4. Stellar mass vs. radius for K2 stars from scaling relations where $\Delta\nu$ (top, Equations 1 and 2) or L (bottom, Equations 3 and 4) are used as an observational constraint. Stars flagged for unreliable $\Delta\nu$ are shown in red (see Section 3.1.1 for a description of the flag). The large black points in the top panel show the effect of decreasing $\Delta\nu$ in steps of 5% and recalculating the mass and radius, for a star of initial mass $1 M_\odot$ and radius $11 R_\odot$. Stellar mass and radius increase with increasing bias on $\Delta\nu$, following the feature seen in the stars flagged for unreliable $\Delta\nu$.

therefore a result of the priors on the mass and age used in our analysis. The bottom panel of Figure 8 shows a comparison between the two where, at M_{scaling} below around $0.7 M_\odot$, we see a deviation caused by the upper limit of the age prior used. We flag stars within 1σ of this limit (20 Gyr), where σ is the median fractional uncertainty of the whole population multiplied by the stellar age (purple points). We choose this estimate as the uncertainties reported on individual stars with posteriors affected by the prior will be artificially small, and this appears to select the affected stars well. We apply the same process to the results constrained by $[T_{\text{eff}}, [\text{Fe}/\text{H}], \nu_{\text{max}}, \Delta\nu]$, though the affected stars are not easily identifiable in a comparison of the masses (top panel) as PARAM uses $\langle \Delta\nu \rangle$ computed using the radial mode frequencies of the models in the grid, so the results are not directly comparable to the scaling relations in this case (see Rodrigues et al. 2017, for details). The results constrained by $\Delta\nu$ are, therefore, an important improvement but, in both cases, the flagged stars are potentially unreliable, and we ensure that the results presented in

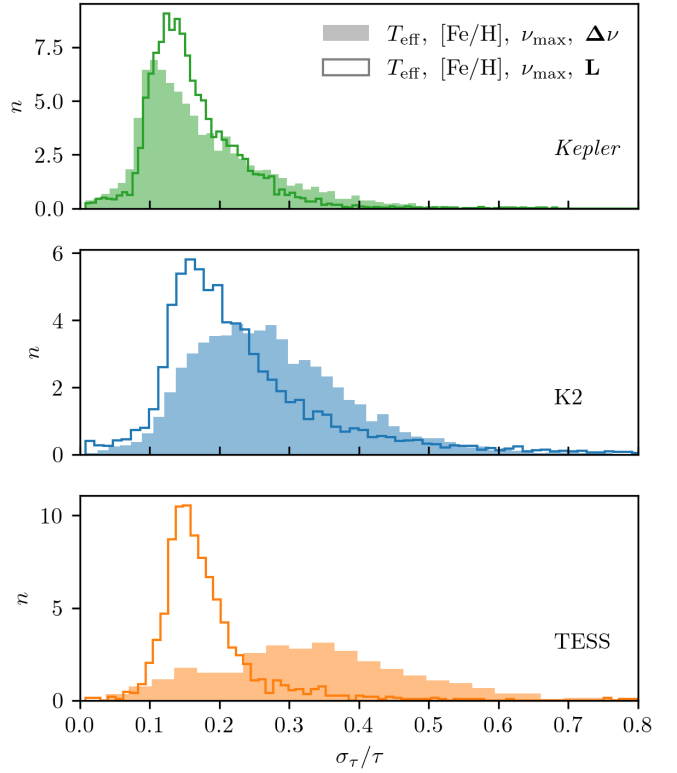


Figure 5. Distribution of the fractional uncertainty on age from PARAM where $\Delta\nu$ (filled) or L (open) are used as an observational constraint for *Kepler* (top), *K2* (middle) and *TESS* (bottom). The area under each histogram integrates to one.

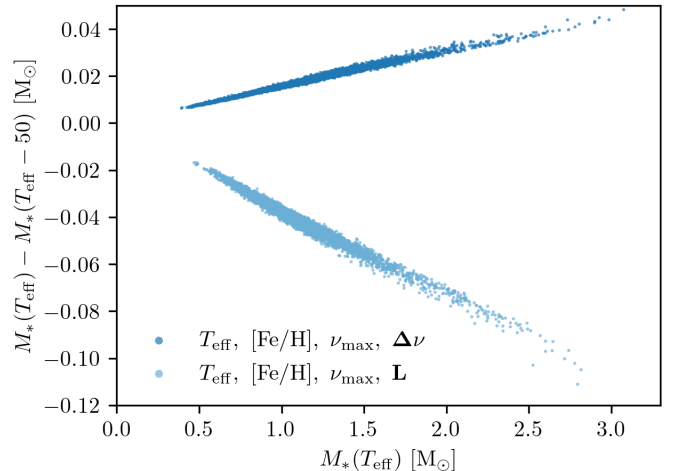


Figure 6. Difference between stellar masses for K2 stars obtained from scaling relations when T_{eff} is shifted by 50 K vs. original mass. The cases where $\Delta\nu$ (dark) or L (light) are used as an observational constraint are shown.

the rest of this paper based on PARAM outputs are not affected by removing them.

With the possible exception of products of partial envelope stripping on the RGB (Li et al. 2022; Matteuzzi et al. 2023, 2024; Mazzia et al. 2025), the majority of stars at these low masses are CHeB (see also their position in the lower panel of Figure 9). These stars are likely to lose significant mass in the upper RGB (Miglio et al.

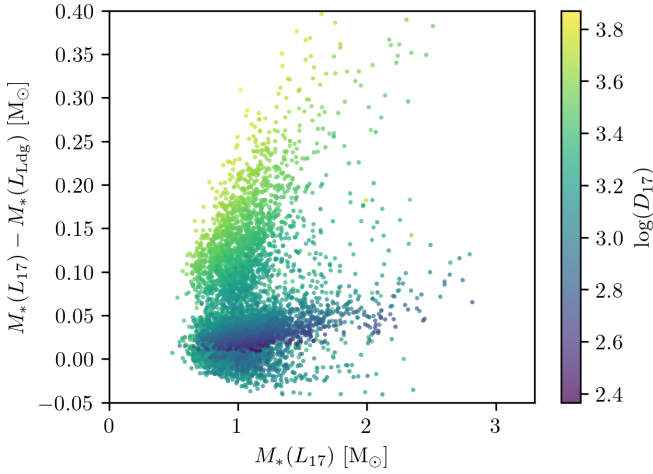


Figure 7. Difference between stellar masses for K2 stars obtained from scaling relations using luminosity when the correction to the *Gaia* parallax zero-point offset is changed from a constant 17 μas (L_{17}) to the correction proposed by Lindegren et al. (2021) (L_{Ldg}). The difference is shown as a function of the L_{17} mass and coloured according to the distance from the inverse of the *Gaia* parallax, with a constant zero-point correction of 17 μas .

2021; Tailo et al. 2021; Brogaard et al. 2024; Li 2025) and reach the CHeB phase with masses that would indicate, if mass-loss were not accounted for, ages much greater than the age of the Universe. Since our current prescription for mass loss is limited (see Section 3.1), we do not consider these stars to have robust ages and remove them from our sample.

The top panel of Figure 9 shows the Hertzsprung-Russell Diagram (HRD) for the sample with stellar parameters based on $\Delta\nu$ using the asteroseismic luminosity L_{seis} ,

$$\frac{L_{\text{seis}}}{L_{\odot}} = \left(\frac{\nu_{\text{max}}}{\nu_{\text{max}, \odot}} \right)^2 \left(\frac{\Delta\nu}{\Delta\nu_{\odot}} \right)^{-4} \left(\frac{T_{\text{eff}}}{T_{\text{eff}, \odot}} \right)^5, \quad (5)$$

and the bottom panel shows stars with parameters from L_{17} . The stars flagged as having unreliable $\Delta\nu$ values are shown in red and those with parameters possibly affected by the age prior are shown in purple. There are fewer prior-affected stars shown in the $\Delta\nu$ results as there is a significant overlap with those stars already removed by the $\Delta\nu$ flag. This means that the results based on $\Delta\nu$ are less sensitive to the prior, but have fewer CHeB stars overall.

3.2 Orbital parameters

Orbital parameters are computed using the fast orbit estimation method of Mackereth & Bovy (2018), implemented in `galpy` (Bovy 2015) and a left-handed Galactocentric coordinate frame. We assume that the MW is well represented by the simple Milky Way potential `MWPotential2014` (Bovy 2015), and that the radial position of the Sun is $R_{\text{Gal}, \odot} = 8.0$ kpc, where the circular velocity is $v_{\text{circ}} = 220 \text{ km s}^{-1}$ (Bovy et al. 2012). The additional solar motion is given by $[U, V, W]_{\odot} = [-11.1, 12.24, 7.25] \text{ km s}^{-1}$ (Schönrich et al. 2010), and the Sun's vertical offset from the Galactic plane is $Z_{\text{Gal}, \odot} = 20.8 \text{ pc}$ (Bennett & Bovy 2019).

To constrain the parameters and their uncertainties, we draw samples from the covariance matrix formed by $[\alpha, \delta, \mu_{\alpha}, \mu_{\delta}]$ (from *Gaia*), RV (from APOGEE or GALAH) and either D from PARAM, when using $\Delta\nu$ to constrain the stellar parameters, or *Gaia* ϖ , when using L . In the latter case, we invert the sampled ϖ to obtain an

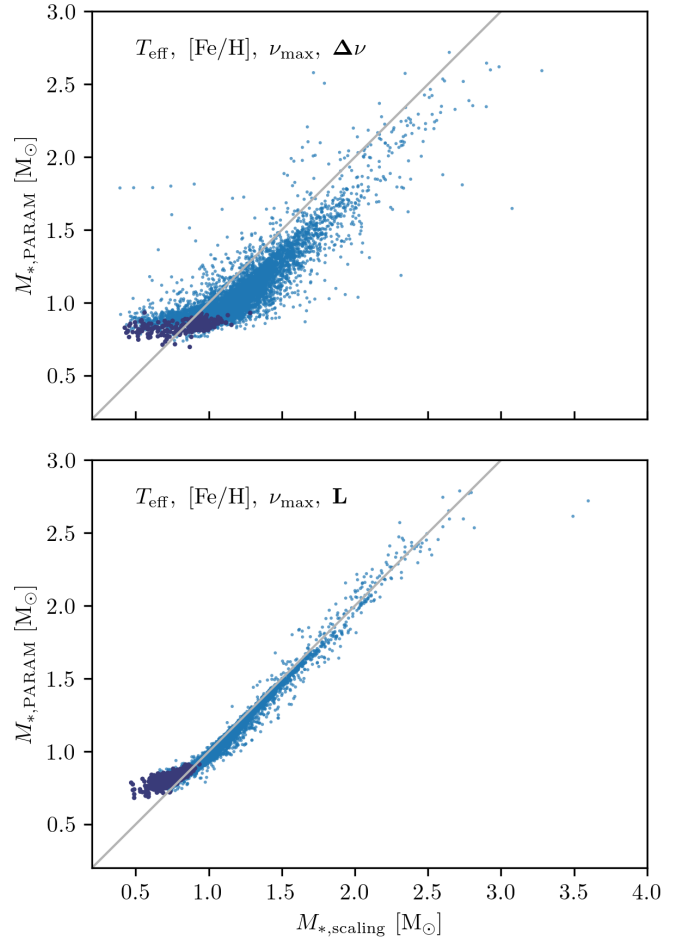


Figure 8. Stellar masses for K2 stars obtained from PARAM vs. those from scaling relations where $\Delta\nu$ (top) or L (bottom) are used as an observational constraint. Stars with masses that may be dominated by the priors imposed in PARAM are shown in purple (see Section 3.1.3 for a description of the flag).

estimate for D . We assume that the spectroscopic RV and D from PARAM are uncorrelated with each other and the other parameters, but in all other cases we utilise the correlation coefficients included in the *Gaia* catalogue. The estimated parameters include the orbital energy, E , angular momentum, L_Z , guiding radius, R_g , maximum vertical excursion, Z_{max} , and eccentricity, e , and report the median and 16th and 84th percentiles.

4 APPLICATIONS

In this section, we demonstrate some applications of the samples presented above. In all cases, we show only stars with reliable ages and, unless otherwise stated, use the stellar parameters from PARAM, constrained by $[T_{\text{eff}}, [\text{Fe}/\text{H}], \nu_{\text{max}}, \Delta\nu]$ and K2 results from the BHM-APOGEE sample. We choose to focus on the ages constrained by $\Delta\nu$ as, though they are less precise for K2 and TESS, the sensitivity to T_{eff} and ϖ -zeropoint is reduced (Section 3.1.2).

4.1 Kinematic properties

First, in Figures 10 and 11 we show two commonly used kinematic planes: the Toomre diagram (velocities in Galactocentric Cartesian

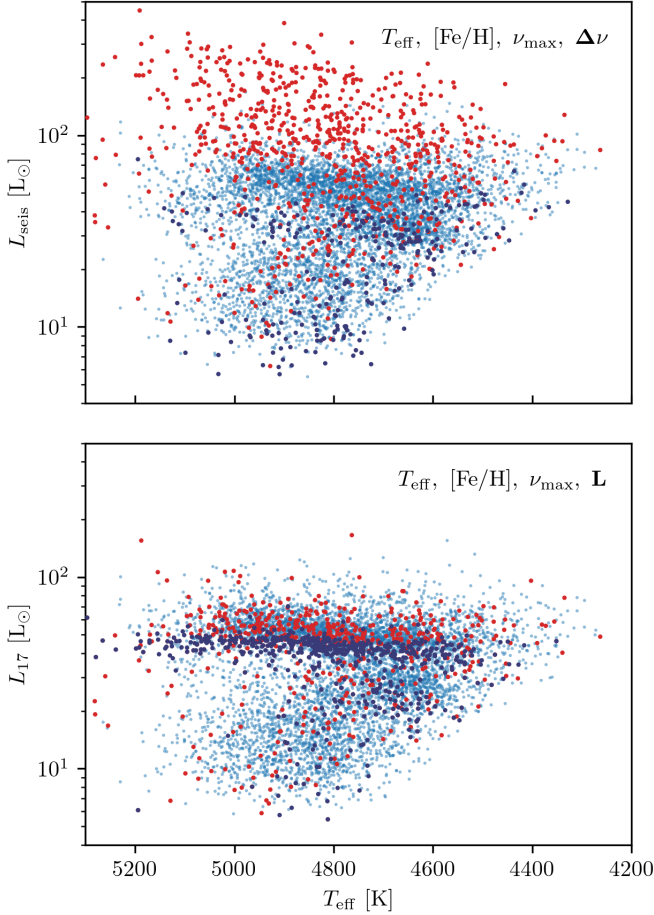


Figure 9. HRD showing K2 stars flagged for unreliable $\Delta\nu$ (red) and with masses that may be dominated by the priors imposed in PARAM are shown (purple; see Section 3.1 for a description of the flags). The full sample is shown in the background (blue).

coordinates) and orbital energy vs. angular momentum. In both planes, we see that the TESS sample is confined to the thin disc, *Kepler* extends into the thick disc and includes a few halo stars, and K2 provides better coverage of the halo (see Figure 10, where the grey line indicates the approximate separation of disc and halo stars). This is consistent with the chemical picture from Figure 3, as the low- and high- α and low-metallicity ($[\text{Fe}/\text{H}] \lesssim -0.7$) populations map well, in broad terms, to the thin and thick discs and halo, respectively. Figure 11 shows that the majority of stars on retrograde orbits which are present in our samples are found in K2, which also provides better coverage of the inner Galaxy (low-energy orbits).

In many applications, it is useful to investigate spatial trends in the Galaxy and in these cases K2 is especially valuable (see Figure 2 for a comparison of the samples' spatial distributions). However, using the present-day positions of stars does not provide the most representative view of the processes at work in the MW, particularly for older stars, as radial migration and vertical heating move stars away from their birth positions (e.g. Schönrich & Binney 2009; Minchev et al. 2013, 2014; Hayden et al. 2015; Frankel et al. 2018, 2020; Vincenzo & Kobayashi 2020; Miglio et al. 2021). This means that stars passing close to the Sun and within our observable limits today were not necessarily born nearby, and nor do they necessarily have orbits similar to the Sun. Figure 12 shows an alternative choice of coordinates, defined below.

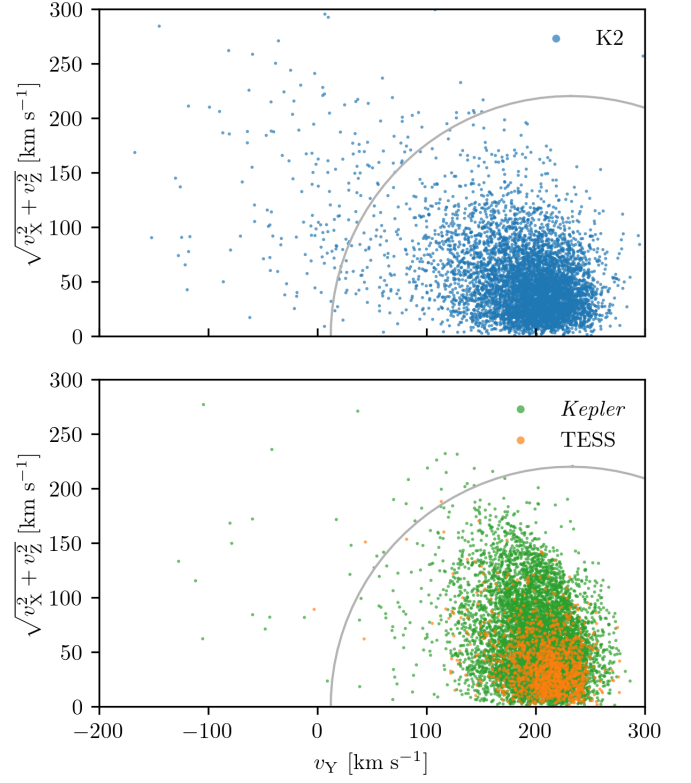


Figure 10. Toomre diagram for stars with reliable ages in the K2 (top), Kepler and TESS (bottom) samples. The grey line indicates the approximate separation of disc and halo stars and the colours are the same as Figure 1.

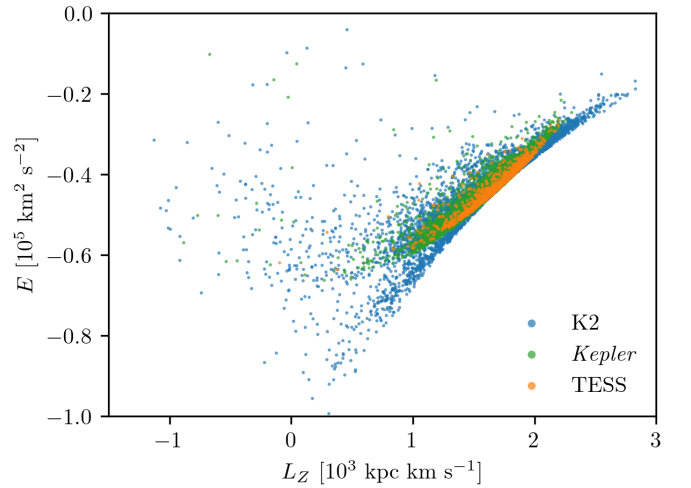


Figure 11. Energy vs. Z-component of angular momentum for stars with reliable ages. The colours are the same as Figure 1.

The term radial migration is used to refer to two processes: blurring, the observational effect of orbital eccentricity, which results in the star being observed at different Galactocentric radii, R_{Gal} , and churning, where interactions with non-axisymmetric features in the Galactic disc result in a change of the orbital radius. Both processes are more important in older populations, as orbital eccentricity tends to increase with time due to radial heating, and the interactions which lead to churning can occur at any time so older stars are more likely

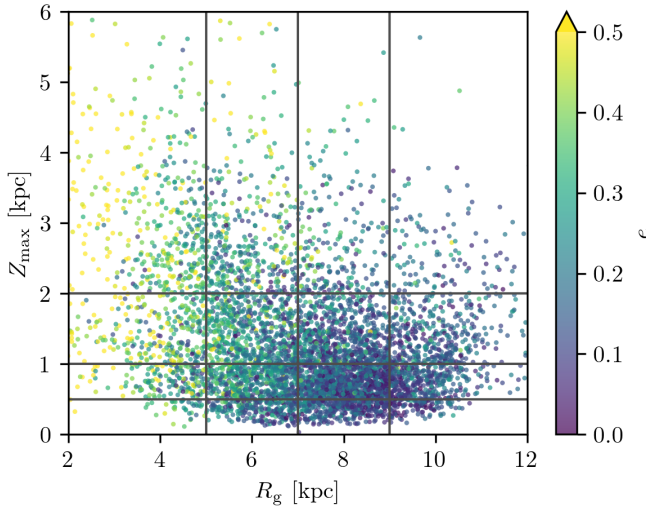


Figure 12. Maximum vertical excursion vs. guiding radius for K2 stars with reliable ages, coloured according to the eccentricity.

to have migrated. The guiding radius R_g , is the radius of a circular orbit with the same L_Z as the true orbit and therefore it mitigates the effect of blurring, providing a better estimate of the ‘average’ radial position of the star. This has the effect of appearing to spread our sample further in radius, as many stars observed around $R_{\text{Gal}} \approx 8$ kpc spend the majority of their orbit closer to or further from the Galactic centre. This is particularly noticeable when comparing the number of stars with R_{Gal} and $R_g \approx 6$ kpc in Figures 2 and 12, where we see many more stars in the latter case, indicating that they are on more eccentric orbits and nearer to apocentre than pericentre.

For the vertical coordinate of Figure 12, it is useful to know how far the orbit extends from the Galactic plane, as this is the main differentiating factor between orbits which are more thin or thick disc-like. The maximum vertical extent of the stellar orbit, Z_{max} , is also expected to increase with time as stars’ orbits are heated by adiabatic (due to the secular evolution of the Galactic disc) or non-adiabatic (due to interactions with other galaxies or giant molecular clouds) processes (Ting & Rix 2019). Figure 12 shows the K2 sample divided into bins in R_g and Z_{max} , which we use to investigate chemical trends later in this section.

It is also useful to investigate how these parameters change as a function of stellar age, as this can throw light on the dynamical evolution of the MW – including radial migration and vertical heating. Figure 13 shows R_g and Z_{max} as a function of stellar mass (which is more precisely constrained than age) and also the distributions of these parameters in six bins of age:

$$\begin{aligned} \tau < 1 \text{ Gyr}, & \quad 1 \text{ Gyr} \leq \tau < 2 \text{ Gyr}, \\ 2 \text{ Gyr} \leq \tau < 4 \text{ Gyr}, & \quad 4 \text{ Gyr} \leq \tau < 6 \text{ Gyr}, \\ 6 \text{ Gyr} \leq \tau < 10 \text{ Gyr}, & \quad 10 \text{ Gyr} \leq \tau. \end{aligned}$$

These age bins increase in width to accommodate the broader age posteriors of older stars. We see clearly that older stars (of lower mass) are distributed over a wider range of both R_g and Z_{max} , and this spread is the signature of churning and vertical heating in our sample.

In Figure 14 we show a similar exercise, using the velocity components in Galactocentric cylindrical coordinates. We see similar trends with age to the previous plot, with older ages corresponding to a larger dispersion. This is a result both of the kinematic heating

experienced by stars in the disc and the fact that the halo population is sampled only in the older bins. The vertical velocity dispersion σ_{vZ} has been studied as an indicator of the MW’s last major merger, as it is expected that this event would have resulted in significant and rapid heating of the MW’s disc at the time (e.g. Helmi et al. 2018; and see also Helmi 2020 and references therein). A simple visual inspection of the data in Figure 14 suggests that the largest change in σ_{vZ} between age bins is between the 4 – 6 Gyr and 6 – 10 Gyr bins (consider the width of the distributions in the bottom right panel), consistent with a merger 10 Gyr ago (e.g. Gallart et al. 2019). However, since the bin width also increases here from two to four Gyr, this indication should be treated with caution and further investigation is needed to confirm whether it can really be attributed to the MW’s merger history.

4.2 Chemical abundances and chemically selected populations

Moving beyond the kinematic properties, Figure 15 shows the $[\alpha/\text{M}]$ vs. $[\text{Fe}/\text{H}]$ plane, in the bins of R_g and Z_{max} shown in Figure 12. The stars are coloured according to their age bin, and the data are sorted to show the youngest stars on top. We see clearly that the low- α sequence is dominated by younger stars and the high- α sequence is formed primarily of stars older than 6 Gyr, but there are a few apparently young stars also present. These are interesting objects and are likely the result of binary evolution and mass accretion, rather than genuinely young (e.g. Chiappini et al. 2015; Martig et al. 2015; Izzard et al. 2018; Jofré et al. 2016, 2023). Grisoni et al. (2024) studied these targets in more detail for this sample, while Miglio et al. (2021) investigated those present in the *Kepler* field, and both works support a scenario where these stars are products of mass transfer. Overall in Figure 15, we see a general trend of older, high- α stars in the inner disc, and younger stars concentrated further from the Galactic centre though, as also shown in Figure 13, old stars are found at all R_g . We also see younger stars concentrated in the plane of the disc, while older stars tend to have orbits which extend to greater vertical distances (though there are still old members of the thin disc visible in our data and e.g. Nepal et al. 2024). This is consistent with the findings of other works in the literature (e.g. Hayden et al. 2015 Figure 4; Imig et al. 2023 Figures 8 and 9).

In Figure 16 we show the age distributions of the high- and low- α sequences, as well as the ‘intermediate’ stars from the higher metallicity region where the sequences appear to overlap (see Figure 3 for the separation of these sequences). We consider only RGB stars, as CHeB stars may have experienced significant mass-loss over their ascent of the RGB, resulting in additional systematic uncertainties in the age since the mass loss process is little understood. We select RGB stars using cuts in L and $\log g$:

$$L < 35 \text{ L}_\odot; \log g > 2.6$$

and CHeB stars:

$$L \geq 35 \text{ L}_\odot; \log g < 2.5,$$

where these selections are not continuous in $\log g$ to reduce cross-contamination between the populations. In both the *Kepler* and K2 samples, the high- α population peaks at ≈ 10 Gyr, the low- α at 6 – 7 Gyr, and the peak of the intermediate population is between the two. The median ages of these populations agree very well between *Kepler* and K2, and the agreement is further improved when we remove the stars flagged as potentially affected too strongly by the age prior (as described in Section 3.1.3). Warfield et al. (2021) compared ages from *Kepler* and K2 asteroseismology and found that the high- α sequence in K2 was younger than in their *Kepler* sample, but this is

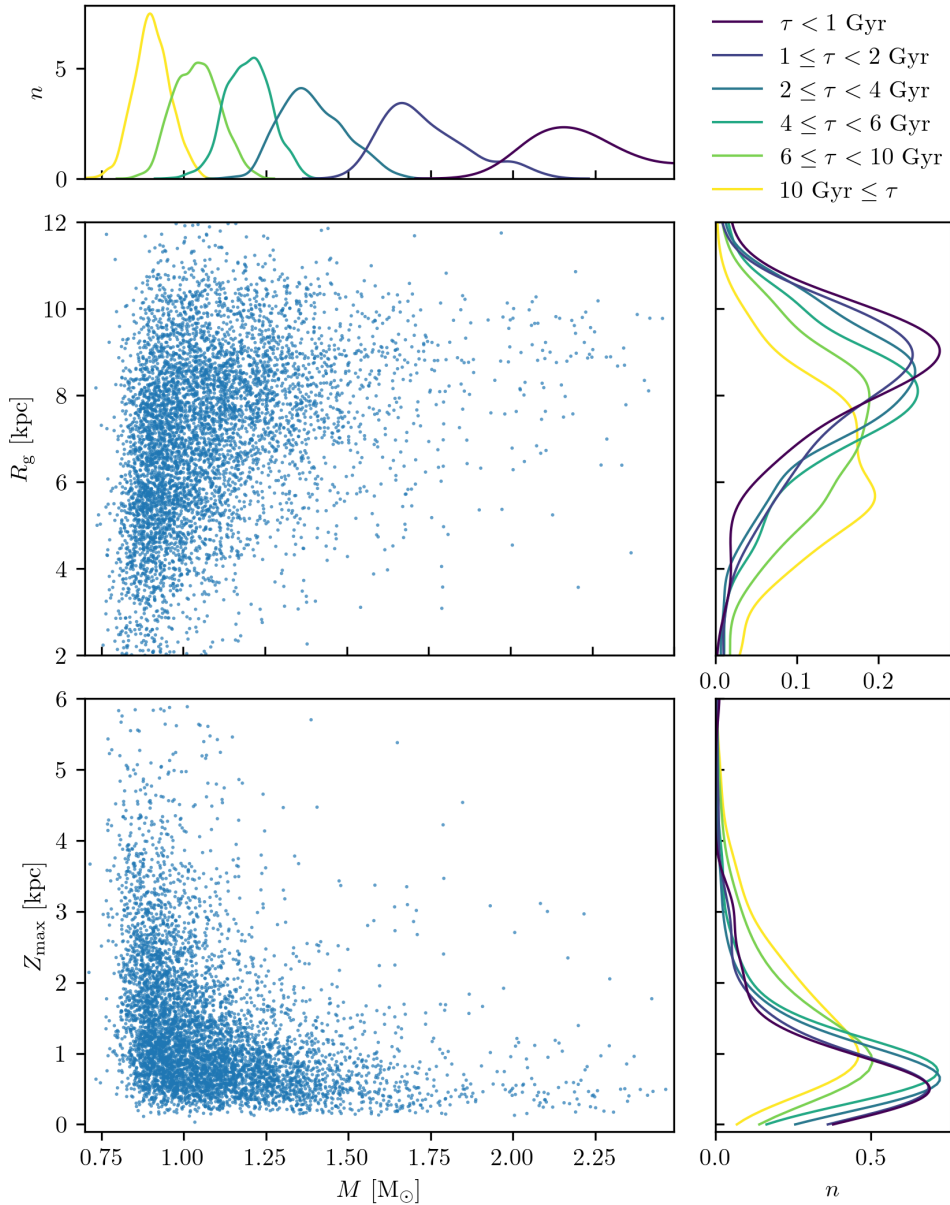


Figure 13. Guiding radius (middle left) and maximum vertical excursion (bottom left) vs. stellar mass for K2 stars with reliable ages. The distributions of M_* (top left), R_g (top right) and Z_{\max} (bottom right) are shown using kernel density estimates in bins of stellar age. The area under each distribution integrates to one.

not the case in our data⁵ and is not present in the revised analysis of Warfield et al. (2024).

Comparing the panels of Figure 16, there appear to be many more high- α stars with ages greater than 10 Gyr present in the K2 sample than *Kepler*. The qualitative differences between these two populations are due to a combination of the larger uncertainties on the ages of the K2 targets (see Figure 5) and their coverage of different Galactic components. Figure 17 shows the v_Z distributions of the same populations. In both *Kepler* and K2, the low- and intermediate- α populations have very similar dispersions: $\sigma_{v_Z} \approx 19 \text{ km s}^{-1}$ in *Kepler* and $\sigma_{v_Z} \approx 22 \text{ km s}^{-1}$ in K2. The high- α populations have a

higher dispersion: $\sigma_{v_Z} \approx 38 \text{ km s}^{-1}$ in *Kepler* and $\sigma_{v_Z} \approx 44 \text{ km s}^{-1}$ in K2. The larger velocity dispersions reflect the difference in the Galactic populations sampled by K2 (e.g. Figure 11 and Gaia Collaboration et al. 2018 Figure 11) and supports the presence of at least some of these very old, kinematically hotter stars, but more precise age information is required to investigate this more robustly.

Figure 18 shows a different separation of the K2 RGB sample and the corresponding age distributions. Hawkins et al. (2015) and Das et al. (2020) proposed the $[\text{Mg}/\text{Mn}]$ vs. $[\text{Al}/\text{Fe}]$ plane as a way of chemically identifying stars with a high probability of having been born outside the MW. These ‘*ex situ*’ stars have high $[\text{Mg}/\text{Mn}]$ and low $[\text{Al}/\text{Fe}]$ (top panel) and lie in the expected low-metallicity, high- α region of the $[\alpha/\text{M}]$ vs. $[\text{Fe}/\text{H}]$ plane (middle panel). We find that they are, on average, slightly younger than the ‘*in situ*’ high- α stars (bottom panel), with a median age of ~ 8.6 Gyr. This is consistent

⁵ Warfield et al. (2021) separation of the high- and low- α sequences would have grouped our intermediate population with the low- α stars, so this cannot explain the difference in our results.

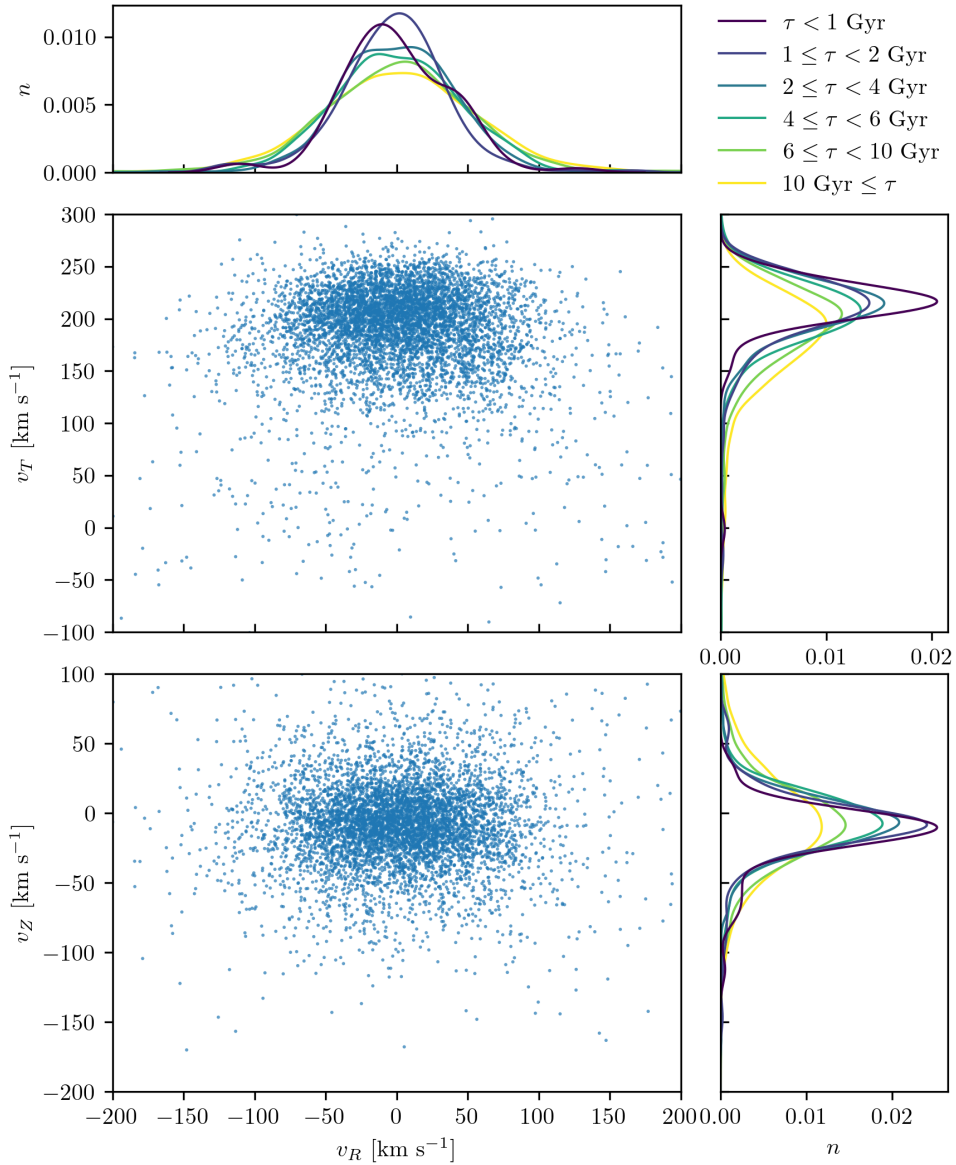


Figure 14. Tangential (middle left) and vertical (bottom left) velocity components vs. radial velocity component for K2 stars with reliable ages. The distributions of v_R (top left), v_T (top right) and v_Z (bottom right) are shown using kernel density estimates in bins of stellar age. The area under each distribution integrates to one.

with literature expectations that the *in situ* high- α population formed with higher star formation efficiency than the *ex situ* (e.g. Hawkins et al. 2014; Gallart et al. 2019; Vincenzo et al. 2019; Das et al. 2020; Montalbán et al. 2021). To further refine the sample of *ex situ* stars, we introduce kinematic information and consider stars with high eccentricity, e , as more likely to have been accreted (e.g. Mackereth et al. 2019a). From the chemically selected population of 18 stars, 6 have $e > 0.7$ with a median age of ~ 8.0 Gyr. The remaining 12 stars (with $e \leq 0.7$) have a median age of ~ 8.8 Gyr. Repeating this analysis for the *Kepler* sample, we find two stars with age ~ 8.8 Gyr.

4.3 Signatures of internal mixing

Results obtained with K2 are also consistent with *Kepler* and TESS when we examine the [C/N] ratio as a function of stellar mass. The observed trend is a well-known consequence of the first dredge-up: by the end of the main sequence (MS) phase, the outer convection zone

gradually extends deeper into the star, bringing to the surface material that has been partially processed by hydrogen burning during the MS phase. Moreover, for more massive stars, surface convection at the first dredge-up affects a larger portion of the star's total mass, leading to a decrease in the [C/N] ratio as the mass on the RGB increases (e.g. Iben 1964, 1967; Masseron & Gilmore 2015; Martig et al. 2016). Figure 19 shows this relationship in the same bins of R_g and Z_{max} used previously, and we see changes across the Galaxy as a result of the different age demographics in each region. The increased scatter at low mass is likely due to variations in initial chemical composition for these old, metal-poor stars (e.g. Kraft 1994; Vincenzo et al. 2021; Roberts et al. 2024). The full K2 sample is shown by the contours in Figure 20, and maps well to the *Kepler* and TESS samples.

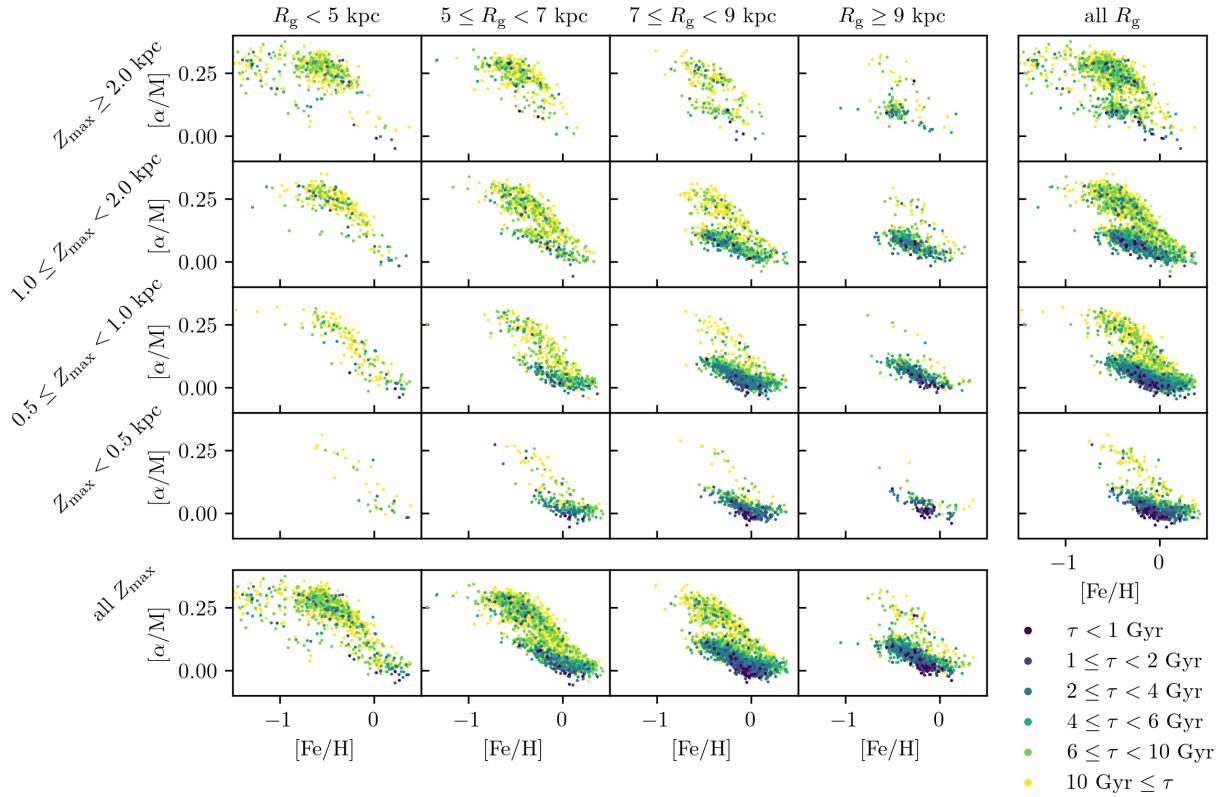


Figure 15. $[\alpha/M]$ vs. $[\text{Fe}/\text{H}]$ in bins of guiding radius and maximum vertical excursion (main panel; as shown in Figure 12) for K2 stars with reliable ages. Also shown are the stars binned only by R_g (bottom panel) or Z_{max} (right panel). Stars are coloured according to age bin.

4.4 Chemical clocks

Finally, in Figure 21, we show four ‘chemical clocks’ as a function of stellar age, from the K2-GALAH sample. Chemical clocks are formed by the ratio of two elements with different nucleosynthesis channels - ideally elements which individually have opposing trends with stellar age (e.g., for RGs in Open Clusters see Slumstrup et al. 2017; Casamiquela et al. 2020, 2021). Identifying and testing consistent and sensitive chemical clocks is a valuable application of stellar ages, as they allow ages to be inferred for large populations of stars where asteroseismic or other age determinations are not available (Moya et al. 2022). Casali et al. (2023) completed a detailed study on chemical clocks using Ce and α -elements in the K2-APOGEE sample, but introducing data from GALAH provides elements from neutron-capture nucleosynthesis channels. Here, we show chemical clocks formed by the s-process elements yttrium and barium (which are not available in APOGEE and have an increase in abundance relative to iron in older stars) compared to the α -element magnesium and the odd-Z element aluminium (which have slightly decreasing trends relative to iron with age). Qualitatively our results agree with those reported in the literature (e.g. Casamiquela et al. 2021), and they demonstrate the utility of the GALAH sample, where elements from more nucleosynthesis channels can be investigated compared to APOGEE. However, though the uncertainties on age and chemical abundances are comparable, we see clearly that detailed analysis is limited by the precision on both axes.

5 SUMMARY AND CONCLUSIONS

We have used asteroseismology based on data from *Kepler*, K2 and TESS, combined with *Gaia* DR3 astrometry and spectroscopic constraints from APOGEE DR17 and GALAH DR3 to infer stellar and orbital parameters for over 17,000 RGs. We pay specific attention to the age estimates of our samples, identifying those which are or may be unreliable for different combinations of observational constraints. In particular, we highlight stars with unreliable $\Delta\nu$ determinations based on comparisons using *Gaia* luminosities. These are particularly relevant in K2 data due to the short duration of the observations of each campaign, and therefore important to characterise for Galactic archaeology studies where the spatial range of K2 is a benefit.

We demonstrate the suitability of different age and mass estimations in different applications including showing trends with age and mass of the orbital parameters R_g and Z_{max} and velocity components, and investigating the $[\alpha/M]$ - $[\text{Fe}/\text{H}]$ plane in bins of R_g , Z_{max} and age. We also compare the age distributions and vertical velocity dispersions of the low- and high- α populations, and the ages obtained from chemically selected *ex situ* stars.

We find that our K2 results agree with the known relationship between stellar mass and $[\text{C}/\text{N}]$ ratio in *Kepler* and TESS, but extend it to lower masses where the other surveys do not sample significantly. We observe greater scatter in this region, which we attribute to the greater spread of initial abundances amongst the oldest stars where the halo population is sampled. Finally, we use abundances from GALAH to show that our K2 ages agree qualitatively with results for chemical clocks based on open clusters.

These datasets, taken together, are a valuable tool for studies of Galactic archaeology and stellar evolution, and the K2 sample pre-

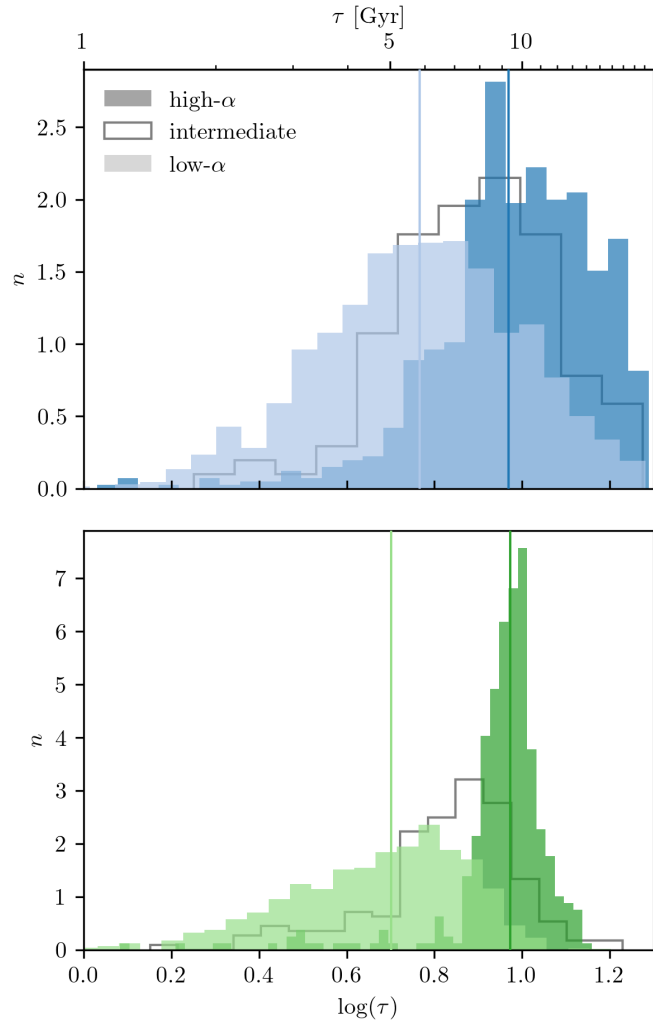


Figure 16. Distributions of logarithmic age for stars in the high- and low- and intermediate α regions of the $[\alpha/\text{M}]$ vs. $[\text{Fe}/\text{H}]$ plane (as shown in Figure 3). The results are shown for likely-RGB stars from K2 (top) and *Kepler* (bottom) with reliable ages (see Section 4.2 for a description of the RGB selection). The area under each histogram integrates to one and the vertical lines show the median age of the low- and high- α populations.

sented here has already been used to investigate open questions in the field of Galactic archaeology, such as the radial metallicity gradient (Willett et al. 2023), Galactic cerium enrichment (Casali et al. 2023) and young α -rich stars (Grisoni et al. 2024), while the *Kepler* and K2 samples have been used to study mass loss during the red-giant-branch phase (Brogaaard et al. 2024).

The examples presented in these works represent a small fraction of the possible applications of these data which offer scope to investigate many open problems directly and to be used as training data which will extend the range of currently available machine learning-based ages.

Looking ahead, the availability of asteroseismology from the continuing TESS mission, as well as future missions including the Nancy Grace Roman Telescope (Spergel et al. 2015) and ESA's PLATO mission (Rauer et al. 2014), will be complemented by future *Gaia* data releases and upcoming spectroscopic surveys (e.g. 4MOST; de Jong et al. 2012, MOONS; Cirasuolo et al. 2014 and WEAVE; Dalton et al. 2020). PLATO, in particular, has the potential to provide age

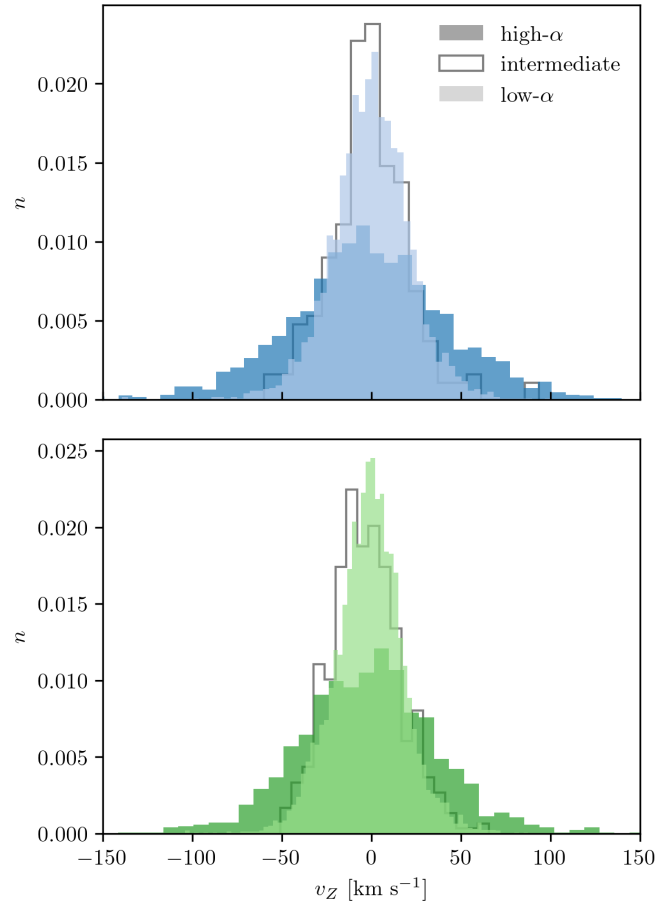


Figure 17. Distributions of vertical velocity for stars in the high- and low- and intermediate α regions of the $[\alpha/\text{M}]$ vs. $[\text{Fe}/\text{H}]$ plane (as shown in Figure 3). The results are shown for likely-RGB stars from K2 (top) and *Kepler* (bottom) with reliable ages (see Section 4.2 for a description of the RGB selection). The area under each histogram integrates to one.

estimates with 10% precision for large samples of RGs (Miglio et al. 2017), which would represent a significant advancement over the present data.

ACKNOWLEDGEMENTS

EW thanks the anonymous reviewer for their helpful comments, which improved the clarity of this paper.

EW, AM, KB, GC, VG, and AS acknowledge support from the ERC Consolidator Grant funding scheme (project ASTEROCHRONOMETRY, G.A. n. 772293 <http://www.asterochronometry.eu>).

SK is funded by the Swiss National Science Foundation through an Eccellenza Professorial Fellowship (award PCEFP2_194638).

VG acknowledges financial support from INAF under the program "Giovani Astrofisiche ed Astrofisici di Eccellenza - IAF: Astrophysics Fellowships in Italy" (Project: GalacticA, "Galactic Archaeology: reconstructing the history of the Galaxy") and INAF Minigrant 2023.

AS has received funding from the European Research Council (ERC) under the European Union's Horizon 2020 research and innovation programme (CartographY; grant agreement ID 804752). DB acknowledges funding support by the Italian Ministerial Grant

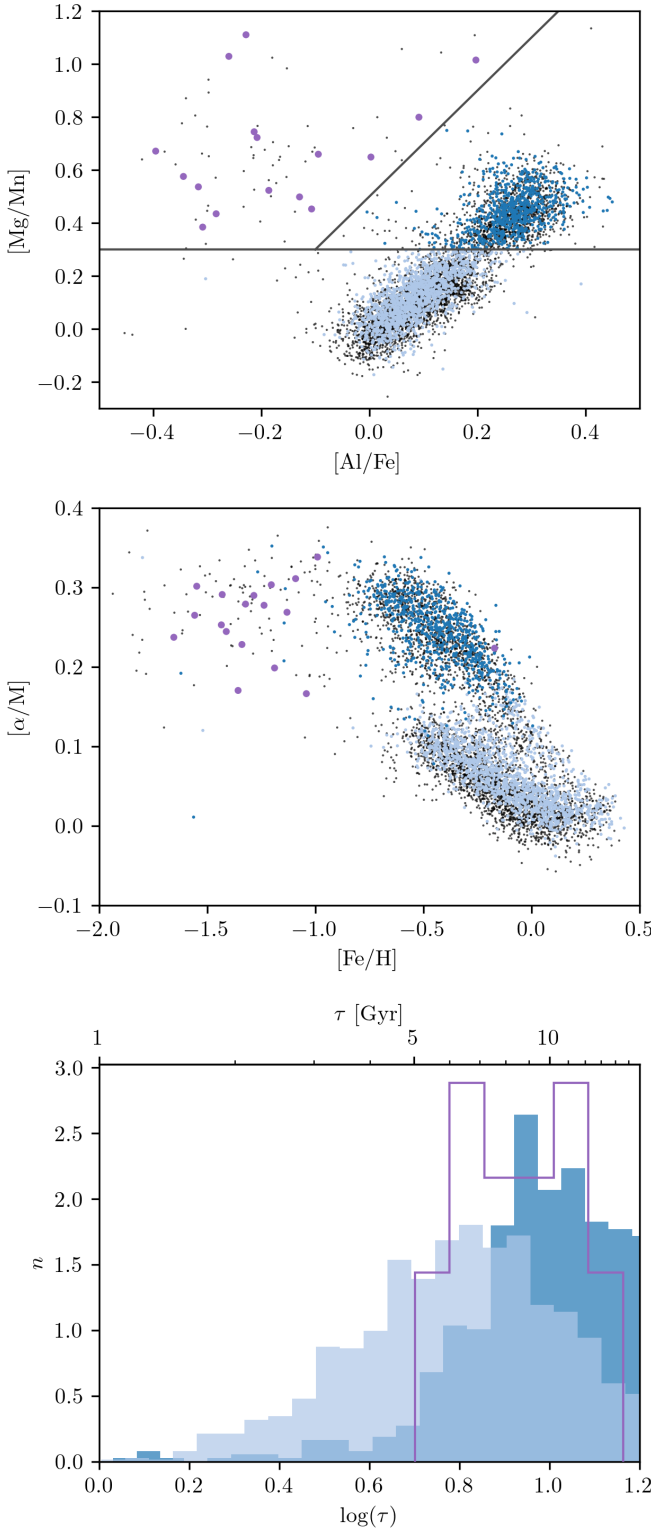


Figure 18. $[\text{Mg}/\text{Mn}]$ vs. $[\text{Al}/\text{Fe}]$ (top) and $[\alpha/\text{Fe}]$ vs. $[\text{Fe}/\text{H}]$ (middle) for K2 stars with reliable ages. Likely-RGB stars are shown in colour in the foreground (see Section 4.2 for a description of the RGB selection) and the full sample is shown in the background (black points). Stars are divided, according to the grey lines in the top panel, into *in situ* low- α (light blue), *in situ* high- α (dark blue) and *ex situ* (purple) populations. Also shown are the distributions of logarithmic age for these three populations (bottom).

PRIN 2022, “Radiative opacities for astrophysical applications”, no. 2022NEXMP8, CUP C53D23001220006.

This paper includes data collected by the Kepler mission and obtained from the MAST data archive at the Space Telescope Science Institute (STScI). Funding for the Kepler mission is provided by the NASA Science Mission Directorate. STScI is operated by the Association of Universities for Research in Astronomy, Inc., under NASA contract NAS 5-26555.

This work has made use of data from the European Space Agency (ESA) mission *Gaia* (<https://www.cosmos.esa.int/gaia>), processed by the *Gaia* Data Processing and Analysis Consortium (DPAC, <https://www.cosmos.esa.int/web/gaia/dpac/consortium>). Funding for the DPAC has been provided by national institutions, in particular the institutions participating in the *Gaia* Multilateral Agreement.

Funding for the Sloan Digital Sky Survey IV has been provided by the Alfred P. Sloan Foundation, the U.S. Department of Energy Office of Science, and the Participating Institutions. SDSS-IV acknowledges support and resources from the Center for High Performance Computing at the University of Utah. The SDSS website is www.sdss4.org. SDSS-IV is managed by the Astrophysical Research Consortium for the Participating Institutions of the SDSS Collaboration including the Brazilian Participation Group, the Carnegie Institution for Science, Carnegie Mellon University, Center for Astrophysics | Harvard & Smithsonian, the Chilean Participation Group, the French Participation Group, Instituto de Astrofísica de Canarias, The Johns Hopkins University, Kavli Institute for the Physics and Mathematics of the Universe (IPMU) / University of Tokyo, the Korean Participation Group, Lawrence Berkeley National Laboratory, Leibniz Institut für Astrophysik Potsdam (AIP), Max-Planck-Institut für Astronomie (MPIA Heidelberg), Max-Planck-Institut für Astrophysik (MPA Garching), Max-Planck-Institut für Extraterrestrische Physik (MPE), National Astronomical Observatories of China, New Mexico State University, New York University, University of Notre Dame, Observatório Nacional / MCTI, The Ohio State University, Pennsylvania State University, Shanghai Astronomical Observatory, United Kingdom Participation Group, Universidad Nacional Autónoma de México, University of Arizona, University of Colorado Boulder, University of Oxford, University of Portsmouth, University of Utah, University of Virginia, University of Washington, University of Wisconsin, Vanderbilt University, and Yale University.

Software: astropy (Astropy Collaboration et al. 2013, 2018, 2022), galpy (Bovy 2015), Matplotlib (Hunter 2007), NumPy (Harris et al. 2020), pandas (pandas development team 2020; McKinney 2010), SciPy (Virtanen et al. 2020) and TOPCAT (Taylor 2005).

DATA AVAILABILITY

The data underlying this article are available online at <https://doi.org/10.5281/zenodo.18417072>.

REFERENCES

- Abdurro'uf et al., 2022, *ApJS*, 259, 35
- Aerts C., 2021, *Reviews of Modern Physics*, 93, 015001
- Anders F., et al., 2017, *A&A*, 600, A70
- Anders F., et al., 2023, *A&A*, 678, A158
- Astropy Collaboration et al., 2013, *A&A*, 558, A33
- Astropy Collaboration et al., 2018, *AJ*, 156, 123
- Astropy Collaboration et al., 2022, *ApJ*, 935, 167
- Bennett M., Bovy J., 2019, *MNRAS*, 482, 1417

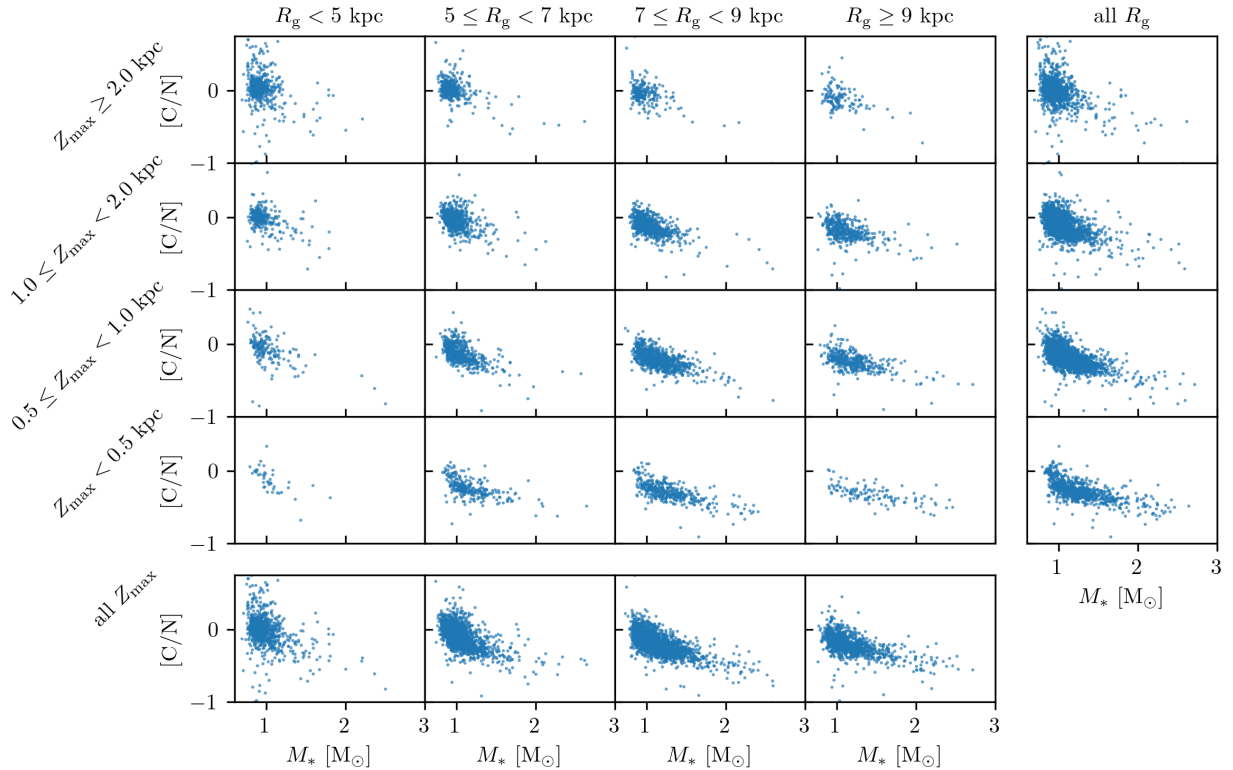


Figure 19. [C/N] vs. stellar mass in bins of guiding radius and maximum vertical excursion (main panel; as shown in Figure 12) for K2 stars with reliable ages. Also shown are the stars binned only by R_g (bottom panel) or Z_{\max} (right panel).

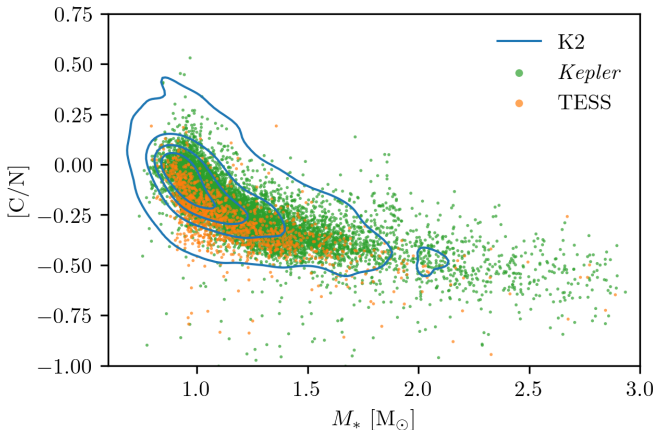


Figure 20. [C/N] vs. stellar mass for *Kepler* (green points), TESS (orange points) and K2 (blue contours) stars with reliable ages.

Borre C. C., et al., 2022, *MNRAS*, **514**, 2527
 Borucki W. J., et al., 2010, *Science*, **327**, 977
 Bovy J., 2015, *ApJS*, **216**, 29
 Bovy J., et al., 2012, *ApJ*, **759**, 131
 Bovy J., Rix H.-W., Green G. M., Schlafly E. F., Finkbeiner D. P., 2016, *ApJ*, **818**, 130
 Brogaard K., Miglio A., van Rossem W. E., Willett E., Thomsen J. S., 2024, *A&A*, **691**, A288
 Brown T. M., Latham D. W., Everett M. E., Esquerdo G. A., 2011, *AJ*, **142**, 112
 Buder S., et al., 2021, *MNRAS*, **506**, 150
 Buder S., et al., 2025, *Publ. Astron. Soc. Australia*, **42**, e051
 Casagrande L., VandenBerg D. A., 2014, *MNRAS*, **444**, 392
 Casagrande L., VandenBerg D. A., 2018, *MNRAS*, **479**, L102
 Casagrande L., et al., 2016, *MNRAS*, **455**, 987
 Casali G., et al., 2023, *A&A*, **677**, A60
 Casamiquela L., Tarricq Y., Soubiran C., Blanco-Cuaresma S., Jofré P., Heiter U., Tucci Maia M., 2020, *A&A*, **635**, A8
 Casamiquela L., et al., 2021, *A&A*, **652**, A25
 Chaplin W. J., Miglio A., 2013, *ARA&A*, **51**, 353
 Chaplin W. J., et al., 2020, *Nature Astronomy*, **4**, 382
 Chiappini C., et al., 2015, *A&A*, **576**, L12
 Cirasuolo M., et al., 2014, in Ramsay S. K., McLean I. S., Takami H., eds, Society of Photo-Optical Instrumentation Engineers (SPIE) Conference Series Vol. 9147, Ground-based and Airborne Instrumentation for Astronomy V. p. 91470N, doi:10.1117/12.2056012
 Ciucă I., Kawata D., Miglio A., Davies G. R., Grand R. J. J., 2021, *MNRAS*, **503**, 2814
 Dalton G., et al., 2020, in Evans C. J., Bryant J. J., Motohara K., eds, Society of Photo-Optical Instrumentation Engineers (SPIE) Conference Series Vol. 11447, Ground-based and Airborne Instrumentation for Astronomy VIII. p. 1144714, doi:10.1117/12.2561067
 Das P., Hawkins K., Jofré P., 2020, *MNRAS*, **493**, 5195
 De Silva G. M., et al., 2015, *MNRAS*, **449**, 2604
 Drimmel R., Cabrera-Lavers A., López-Corredoira M., 2003, *A&A*, **409**, 205
 Elsworth Y., Theibl N., Hekker S., Chaplin W., 2020, *Research Notes of the American Astronomical Society*, **4**, 177
 Frankel N., Rix H.-W., Ting Y.-S., Ness M., Hogg D. W., 2018, *ApJ*, **865**, 96
 Frankel N., Sanders J., Ting Y.-S., Rix H.-W., 2020, *ApJ*, **896**, 15
 Freeman K., Bland-Hawthorn J., 2002, *ARA&A*, **40**, 487
 Gaia Collaboration et al., 2016, *A&A*, **595**, A1
 Gaia Collaboration et al., 2018, *A&A*, **616**, A11
 Gaia Collaboration et al., 2023, *A&A*, **674**, A1
 Gallart C., Bernard E. J., Brook C. B., Ruiz-Lara T., Cassisi S., Hill V., Monelli M., 2019, *Nature Astronomy*, **3**, 932
 García Pérez A. E., et al., 2016, *AJ*, **151**, 144
 Gilliland R. L., et al., 2010, *PASP*, **122**, 131

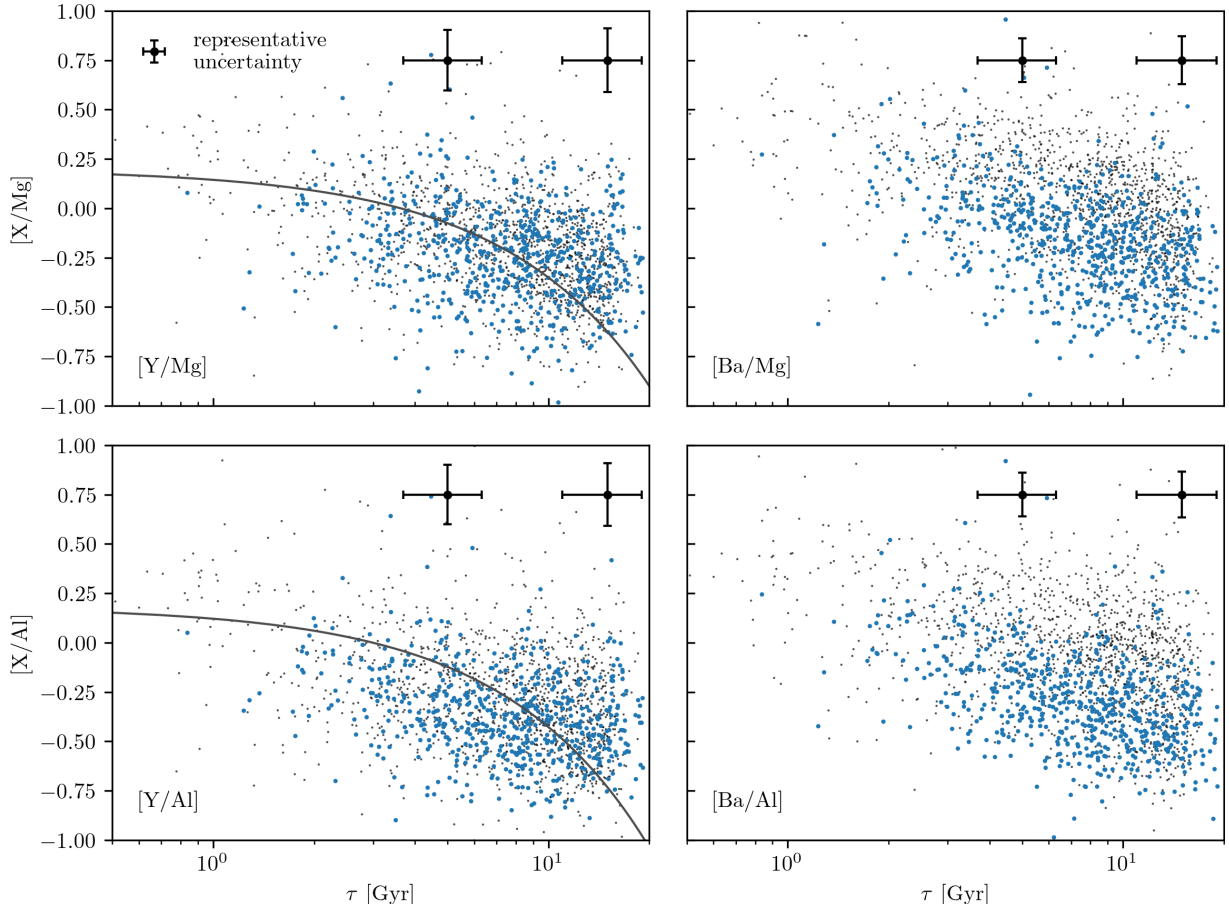


Figure 21. Abundance ratios vs. age for four elements commonly used in chemical clocks, from different nucleosynthetic channels: yttrium (left; light s-process), barium (right; heavy s-process), magnesium (top; α element) and aluminium (bottom; odd-Z element). The stars shown have reliable ages from the K2-GALAH cross-match and the likely-RGB sample is shown in blue points in the foreground. The black errorbars show median uncertainties on age and chemical abundance of stars younger (left point) or older (right point) than 10 Gyr. The grey line shows the relationship between the yttrium chemical clocks and age found by Casamiquela et al. (2021).

Green G. M., 2018, *The Journal of Open Source Software*, **3**, 695
 Green G. M., et al., 2014, *ApJ*, **783**, 114
 Green G. M., Schlafly E., Zucker C., Speagle J. S., Finkbeiner D., 2019, *ApJ*, **887**, 93
 Grisoni V., et al., 2024, *A&A*, **683**, A111
 Grunblatt S. K., et al., 2021, *ApJ*, **916**, 88
 Hall O. J., et al., 2021, *Nature Astronomy*, **5**, 707
 Harris C. R., et al., 2020, *Nature*, **585**, 357
 Hawkins K., Jofré P., Gilmore G., Masseron T., 2014, *MNRAS*, **445**, 2575
 Hawkins K., Jofré P., Masseron T., Gilmore G., 2015, *MNRAS*, **453**, 758
 Hayden M. R., et al., 2015, *ApJ*, **808**, 132
 Hegedűs V., Mészáros S., Jofré P., Stringfellow G. S., Feuillet D., García-Hernández D. A., Nitschelm C., Zamora O., 2023, *A&A*, **670**, A107
 Helmi A., 2020, *ARA&A*, **58**, 205
 Helmi A., Babusiaux C., Koppelman H. H., Massari D., Veljanoski J., Brown A. G. A., 2018, *Nature*, **563**, 85
 Hon M., Stello D., Yu J., 2018a, *MNRAS*, **476**, 3233
 Hon M., Stello D., Zinn J. C., 2018b, *ApJ*, **859**, 64
 Howell S. B., et al., 2014, *PASP*, **126**, 398
 Huber D., et al., 2016, *ApJS*, **224**, 2
 Hunter J. D., 2007, *Computing in Science and Engineering*, **9**, 90
 Iben Jr. I., 1964, *ApJ*, **140**, 1631
 Iben Jr. I., 1967, *ApJ*, **147**, 624
 Imig J., et al., 2023, *ApJ*, **954**, 124
 Izzard R. G., Preece H., Jofré P., Halabi G. M., Masseron T., Tout C. A., 2018, *MNRAS*, **473**, 2984
 Jofré P., et al., 2016, *A&A*, **595**, A60
 Jofré P., et al., 2023, *A&A*, **671**, A21
 Khan S., et al., 2023, *A&A*, **677**, A21
 Kos J., et al., 2017, *MNRAS*, **464**, 1259
 Kraft R. P., 1994, *PASP*, **106**, 553
 Leung H. W., Bovy J., Mackereth J. T., Miglio A., 2023, *MNRAS*, **522**, 4577
 Li Y., 2025, *ApJ*, **988**, 179
 Li Y., et al., 2022, *Nature Astronomy*, **6**, 673
 Li Y., et al., 2023, *MNRAS*, **523**, 916
 Lindegren L., 2018, Re-normalising the astrometric chi-square in Gaia DR2, GAIA-C3-TN-LU-LL-124, http://www.rssd.esa.int/doc_fetch.php?id=3757412
 Lindegren L., et al., 2021, *A&A*, **649**, A4
 Luger R., Kruse E., Foreman-Mackey D., Agol E., Saunders N., 2018, *AJ*, **156**, 99
 Mackereth J. T., Bovy J., 2018, *PASP*, **130**, 114501
 Mackereth J. T., et al., 2019a, *MNRAS*, **482**, 3426
 Mackereth J. T., et al., 2019b, *MNRAS*, **489**, 176
 Mackereth J. T., et al., 2021, *MNRAS*, **502**, 1947
 Majewski S. R., et al., 2017, *AJ*, **154**, 94
 Marrese P. M., Marinoni S., Fabrizio M., Altavilla G., 2022, Technical Report 15, Gaia DR3 documentation Chapter 15: Cross-match with external catalogues
 Marshall D. J., Robin A. C., Reylé C., Schultheis M., Picaud S., 2006, *A&A*, **453**, 635
 Martig M., et al., 2015, *MNRAS*, **451**, 2230

Martig M., et al., 2016, *MNRAS*, **456**, 3655
 Masseron T., Gilmore G., 2015, *MNRAS*, **453**, 1855
 Matsuno T., et al., 2021, *ApJ*, **912**, 72
 Matteucci F., 2021, *A&ARv*, **29**, 5
 Matteuzzi M., et al., 2023, *A&A*, **671**, A53
 Matteuzzi M., Hendriks D., Izzard R. G., Miglio A., Brogaard K., Montalbán J., Tailo M., Mazzi A., 2024, *A&A*, **691**, A17
 Mazzi A., Thomsen J. S., Miglio A., Brogaard K., Girardi L., Bossini D., Matteuzzi M., van Rossem W. E., 2025, *A&A*, **699**, A39
 McKinney W., 2010, in Stéfan van der Walt Jarrod Millman eds, Proceedings of the 9th Python in Science Conference. pp 56 – 61, doi:10.25080/Majora-92bf1922-00a
 Miglio A., et al., 2012, *MNRAS*, **419**, 2077
 Miglio A., et al., 2013, in European Physical Journal Web of Conferences. EDP, p. 03004 (arXiv:1301.1515), doi:10.1051/epjconf/20134303004
 Miglio A., et al., 2017, *Astronomische Nachrichten*, **338**, 644
 Miglio A., et al., 2021, *A&A*, **645**, A85
 Minchev I., Chiappini C., Martig M., 2013, *A&A*, **558**, A9
 Minchev I., Chiappini C., Martig M., 2014, *A&A*, **572**, A92
 Montalbán J., et al., 2021, *Nature Astronomy*, **5**, 640
 Mora A., González-Núñez J., Utrilla E., Ríos Diaz C., 2022, Technical Report 16, Gaia DR3 documentation Chapter 16: Cross-match with Gaia DR2
 Morel T., Creevey O. L., Montalbán J., Miglio A., Willett E., 2021, *A&A*, **646**, A78
 Mosser B., Appourchaux T., 2009, *A&A*, **508**, 877
 Mosser B., et al., 2010, *A&A*, **517**, A22
 Moya A., Sarro L. M., Delgado-Mena E., Chaplin W. J., Adibekyan V., Blanco-Cuaresma S., 2022, *A&A*, **660**, A15
 Nepal S., Chiappini C., Queiroz A. B., Guiglion G., Montalbán J., Steinmetz M., Miglio A., Khalatyan A., 2024, *A&A*, **688**, A167
 Paxton B., Bildsten L., Dotter A., Herwig F., Lesaffre P., Timmes F., 2011, *ApJS*, **192**, 3
 Paxton B., et al., 2013, *ApJS*, **208**, 4
 Paxton B., et al., 2015, *ApJS*, **220**, 15
 Paxton B., et al., 2018, *ApJS*, **234**, 34
 Paxton B., et al., 2019, *ApJS*, **243**, 10
 Rauer H., et al., 2014, *Experimental Astronomy*, **38**, 249
 Reimers D., 1975, *Memoires of the Societe Royale des Sciences de Liege*, **8**, 369
 Rendle B. M., et al., 2019, *MNRAS*, **490**, 4465
 Ricker G. R., et al., 2015, *Journal of Astronomical Telescopes, Instruments, and Systems*, **1**, 014003
 Roberts J. D., et al., 2024, *MNRAS*, **530**, 149
 Rodrigues T. S., et al., 2014, *MNRAS*, **445**, 2758
 Rodrigues T. S., et al., 2017, *MNRAS*, **467**, 1433
 Salaris M., Chieffi A., Straniero O., 1993, *ApJ*, **414**, 580
 Schonhut-Stasik J., et al., 2024, *AJ*, **167**, 50
 Schönrich R., Binney J., 2009, *MNRAS*, **396**, 203
 Schönrich R., Binney J., Dehnen W., 2010, *MNRAS*, **403**, 1829
 Sharma S., et al., 2019, *MNRAS*, **490**, 5335
 Sharma S., Stello D., Zinn J. C., Reyes C., Hon M., Bland-Hawthorn J., 2022, *MNRAS*, **517**, 1970
 Silva Aguirre V., et al., 2018, *MNRAS*, **475**, 5487
 Skrutskie M. F., et al., 2006, *AJ*, **131**, 1163
 Slumstrup D., Grundahl F., Brogaard K., Thygesen A. O., Nissen P. E., Jessen-Hansen J., Van Eylen V., Pedersen M. G., 2017, *A&A*, **604**, L8
 Spergel D., et al., 2015, arXiv e-prints, p. arXiv:1503.03757
 Stokholm A., Aguirre Børseth-Koch V., Stello D., Hon M., Reyes C., 2023, *MNRAS*, **524**, 1634
 Tailo M., et al., 2021, *MNRAS*, **503**, 694
 Tailo M., et al., 2022, *A&A*, **662**, L7
 Taylor M. B., 2005, in Shopbell P., Britton M., Ebert R., eds, *Astronomical Society of the Pacific Conference Series* Vol. 347, *Astronomical Data Analysis Software and Systems XIV*. p. 29
 Ting Y.-S., Rix H.-W., 2019, *ApJ*, **878**, 21
 Valentini M., et al., 2019, *A&A*, **627**, A173

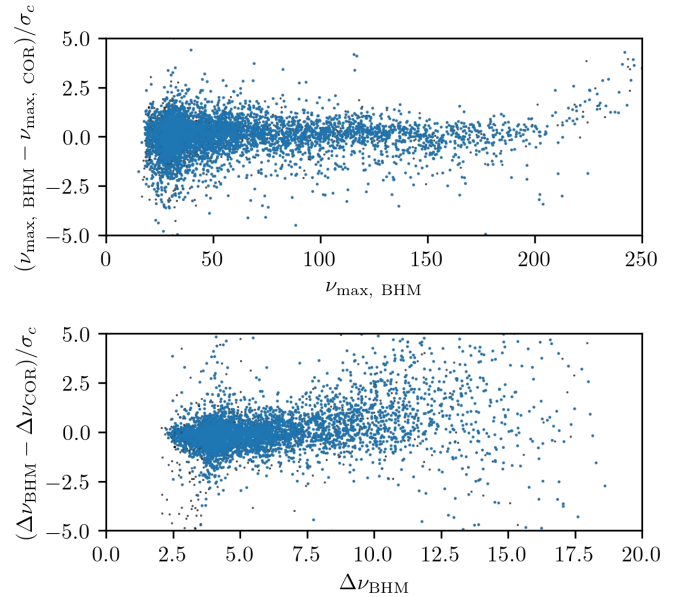


Figure A1. Difference between ν_{\max} (top) and $\Delta\nu$ (bottom) for K2 stars from BHM and COR pipelines, relative to combined uncertainty. Stars with reliable ages are shown in the foreground with blue points. Stars with reliable data but which do not pass our tests on age are shown as black points in the background. For clarity, we have not shown the few ($< 1\%$ in ν_{\max} and $< 5\%$ in $\Delta\nu$) stars where the disagreements exceed $5\sigma_c$.

Valle G., Dell’Omodarme M., Prada Moroni P. G., Degl’Innocenti S., 2024, *A&A*, **685**, A150
 Vincenzo F., Kobayashi C., 2020, *MNRAS*, **496**, 80
 Vincenzo F., Spitoni E., Calura F., Matteucci F., Silva Aguirre V., Miglio A., Cescutti G., 2019, *MNRAS*, **487**, L47
 Vincenzo F., et al., 2021, arXiv e-prints, p. arXiv:2106.03912
 Virtanen P., et al., 2020, *Nature Medicine*, **17**, 261
 Warfield J. T., et al., 2021, *AJ*, **161**, 100
 Warfield J. T., et al., 2024, *AJ*, **167**, 208
 Willett E., et al., 2023, *MNRAS*, **526**, 2141
 Yu J., Huber D., Bedding T. R., Stello D., Hon M., Murphy S. J., Khanna S., 2018, *ApJS*, **236**, 42
 da Silva L., et al., 2006, *A&A*, **458**, 609
 de Jong R. S., et al., 2012, in McLean I. S., Ramsay S. K., Takami H., eds, *Society of Photo-Optical Instrumentation Engineers (SPIE) Conference Series* Vol. 8446, *Ground-based and Airborne Instrumentation for Astronomy IV*. p. 84460T (arXiv:1206.6885), doi:10.1117/12.926239
 pandas development team T., 2020, pandas-dev/pandas: Pandas, doi:10.5281/zenodo.3509134, <https://doi.org/10.5281/zenodo.3509134>

APPENDIX A: ASTEROSEISMIC PIPELINE COMPARISON FOR K2 TARGETS

Figure A1 shows a comparison of the asteroseismic parameters obtained for K2 stars from the independent BHM and COR pipelines, relative to their combined uncertainty. In general, the pipelines agree at the 2σ level.

APPENDIX B: IDENTIFYING NYQUIST-AFFECTED ν_{\max}

Figure B1 shows stars removed from the K2-BHM-APOGEE sample due to cuts on the asteroseismic parameters as red points. Targets with

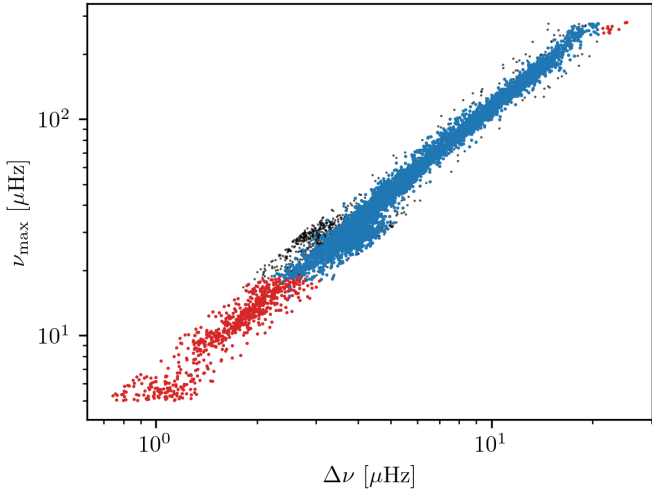


Figure B1. ν_{\max} vs. $\Delta\nu$ for the K2-BHM-APOGEE sample. Stars removed as a result of the cuts described in Section 2.1.4 are shown in red. Stars with reliable ages based on $\Delta\nu$ (see Section 3.1.1 for a description of the criteria) are shown in blue.

$\nu_{\max} + 3\sigma_{\nu_{\max}} < 20 \mu\text{Hz}$ and $\Delta\nu \geq 21 \mu\text{Hz}$ are rejected, as described in Section 2.1.4.

APPENDIX C: CATALOGUE DESCRIPTION

The columns included in the catalogues released with this work are described in Table C1

APPENDIX D: COMPARING $\Delta\nu$ AND L RESULTS IN KEPLER AND TESS

Figures D1 and D2 show the stellar mass and radius obtained from scaling relations for *Kepler* and TESS stars, with stars flagged as having unreliable $\Delta\nu$ according to the definition in Section 3.1.1 highlighted (red points). In comparison to Figure 4, we see a greatly reduced number of stars highlighted by this flag, as a result of the increased duration of the observations. In K2, 782 stars with otherwise reliable data are removed on the basis of this cut (11%), in *Kepler* and TESS 66 (0.8%) and 72 (5%) stars are removed, respectively.

APPENDIX E: COMPARISON OF AGES TO THE APO-K2 CATALOGUE

Warfield et al. (2024) presented ages for 4661 RGB and a further 1912 RC stars, with evolutionary states based on spectroscopy, described in Warfield et al. (2021). In Figures E1 and E2, we show a comparison of the reliable ages constrained by $[T_{\text{eff}}, [\text{Fe}/\text{H}], \nu_{\max}, \Delta\nu]$ from the BHM-APOGEE sample and those from APO-K2. There are 2989 stars in common with the APO-K2 RGB sample, and 939 in the RC.

This paper has been typeset from a $\text{TeX}/\text{\LaTeX}$ file prepared by the author.

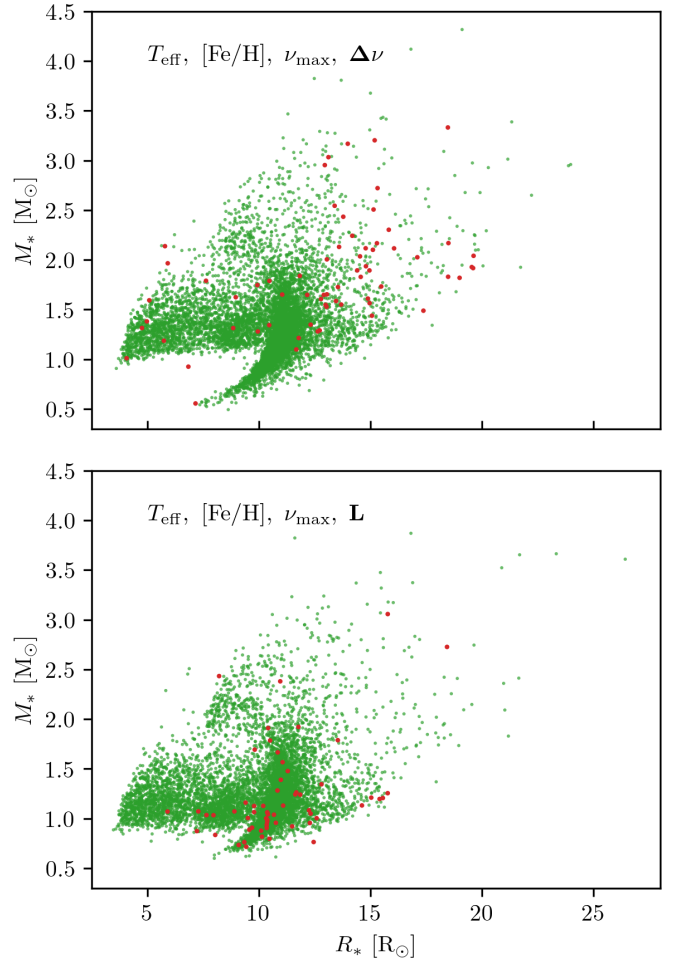


Figure D1. Same as Figure 4, but for *Kepler* targets.

Table C1. Datamodel of the catalogues released with this work.

Column Name	Suffixes	Details	Units
K2_ID/			
KIC_ID/		K2/ <i>Kepler</i> / TESS identifier	
TESS_ID			
K2_Campaign		K2 campaign number (K2 Catalogues only)	
APOGEE_ID/			
GALAH_ID		Spectroscopic survey identifier	
ASPCAP_ID			
GaiaDR3_ID			
numax	add _err for uncertainty then add _BHM or _COR for pipeline (K2 APOGEE catalogue only)	Frequency of maximum oscillation power	μHz
Dnu	-"-	Large frequency separation	μHz
EvoState		From Yu et al. (2018). RGB = 1, HeB = 2, unclassified = 0 (<i>Kepler</i> catalogue only)	
L	add _err for uncertainty then add _plax or _seis	Luminosity based on <i>Gaia</i> parallax or asteroseismology 17 μHz zeropoint correction used in K2 catalogues and Lindegren correction in <i>Kepler</i> and TESS (see Section 2.2)	L_{\odot}
Rg	add _L for 16th or _U for 84th percentile then add _BHM or _Gaia for distance (K2 APOGEE catalogue only)	Guiding radius in MWPotential2014	kpc
Zmax	-"-	Maximum vertical excursion in MWPotential2014	kpc
ecc	-"-	Orbital eccentricity in MWPotential2014	
Lz	-"-	Orbital angular momentum in MWPotential2014	kpc km s^{-1}
Energy	-"-	Orbital energy in MWPotential2014	$\text{km}^2 \text{s}^{-2}$
vR	-"-	Radial velocity component in MWPotential2014	km s^{-1}
vT	-"-	Tangential velocity component in MWPotential2014	km s^{-1}
vZ	-"-	Vertical velocity component in MWPotential2014	km s^{-1}
age	add _L for 16th or _U for 84th percentile then add _Dnu or _L for source of observational constraints (see Section 3.1.1)	Age from PARAM based on BHM and spectroscopy	Gyr
Mass	-"-	Mass from PARAM based on BHM and spectroscopy	M_{\odot}
Radius	-"-	Radius from PARAM based on BHM and spectroscopy	R_{\odot}
Dist	-"-	Distance from PARAM based on BHM and spectroscopy	kpc
warn_low_numax	add _BHM or _COR for pipeline (K2 APOGEE catalogue only)	v_{max} more than three standard deviations below 20 μHz	
warn_high_Dnu	-"-	$\Delta\nu \geq 21 \mu\text{Hz}$	
warn_high_RUWE		from <i>Gaia</i> DR3	
warn_NSS		-"-	
warn_APOGEE/		Combination of flags from spectroscopy (see Section 2.3)	
warn_GALAH			
drop_K2_dup	-"-	Duplicate target removed (K2 catalogues only)	
warn_plax_err		$\varpi/\sigma_{\varpi} < 5$	
warn_dustmaps		Validity of dustmap outputs	
Rel_data	add _BHM or _COR for pipeline (K2 APOGEE catalogue only)	combines flags warn_low_numax to drop_K2_dup for $\Delta\nu$ datasets	
warn_nveAv	add _Dnu or _L for source of observational constraints	or warn_low_numax to warn_dustmaps for L datasets to return stars with reliable data	
warn_massDiff		PARAM returns negative extinction	
Rel_age	add _BHM or _COR for pipeline (K2 APOGEE catalogue only)	Difference in mass from scaling relations based on L or $\Delta\nu$ exceeds 50% (See Section 3.1.1)	
		combines Rel_data with warn_nveAv and warn_massDiff to return stars with reliable ages	

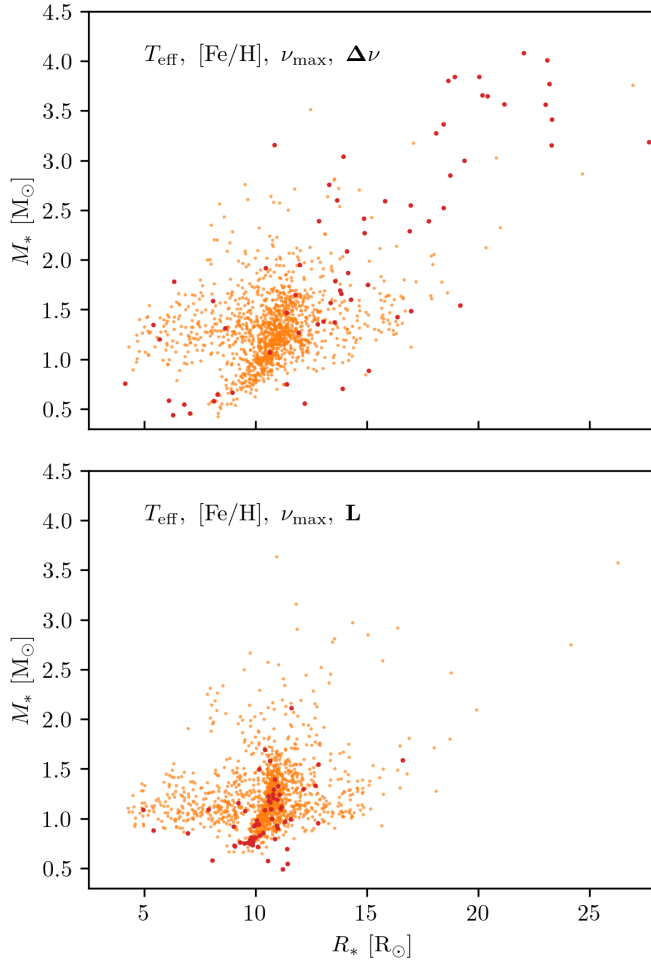


Figure D2. Same as Figure 4, but for TESS targets.

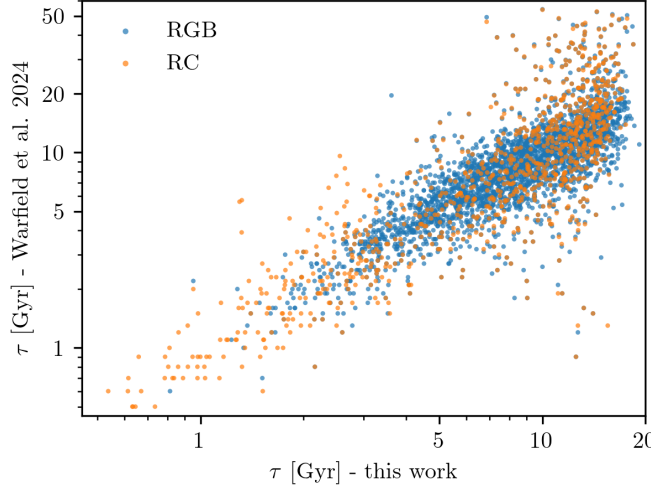


Figure E1. Comparison of ages for stars in common between this work and the APO-K2 catalogue. Evolutionary states are taken from [Warfield et al. \(2024\)](#).

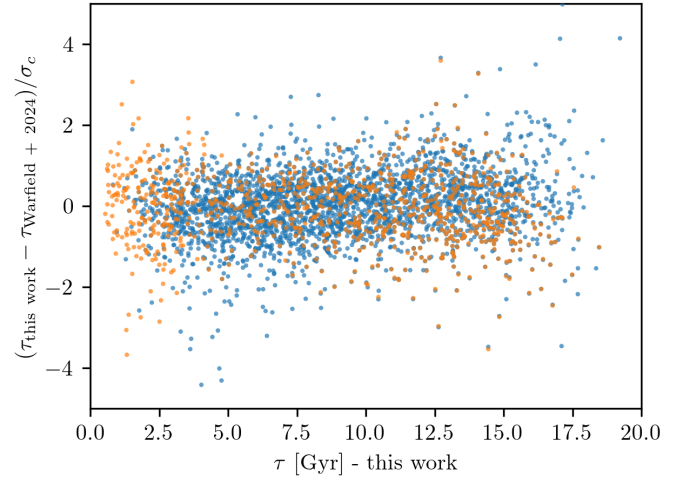


Figure E2. Difference between the ages presented in this work and those from APO-K2, relative to combined uncertainty. The colours are the same as Figure E1. For clarity, three stars which agree at the $5 - 15\sigma$ level are not shown.